Monthly Notices
of the
ROYAL ASTRONOMICAL SOCIETY

MNRAS **468,** 3949–3964 (2017)
Advance Access publication 2017 April 1

doi:10.1093/mnras/stx678

The SLUGGS survey: dark matter fractions at large radii and assembly epochs of early-type galaxies from globular cluster kinematics

Adebusola B. Alabi,[1]★ Duncan A. Forbes,[1]★ Aaron J. Romanowsky,[2,3] Jean P. Brodie,[3] Jay Strader,[4] Joachim Janz,[1] Christopher Usher,[5] Lee R. Spitler,[6,7,8] Sabine Bellstedt[1] and Anna Ferré-Mateu[1]

[1]*Centre for Astrophysics and Supercomputing, Swinburne University, Hawthorn VIC 3122, Australia*
[2]*Department of Physics and Astronomy, San José State University, San Jose, CA 95192, USA*
[3]*University of California Observatories, 1156 High Street, Santa Cruz, CA 95064, USA*
[4]*Department of Physics and Astronomy, Michigan State University, East Lansing, MI 48824, USA*
[5]*Astrophysics Research Institute, Liverpool John Moores University, Liverpool L3 5RF, UK*
[6]*Australian Astronomical Observatory, PO Box 915, North Ryde, NSW 1670, Australia*
[7]*Department of Physics and Astronomy, Macquarie University, North Ryde, NSW 2109, Australia*
[8]*Research Centre for Astronomy, Astrophysics and Astrophotonics, Macquarie University, North Ryde, NSW 2109, Australia*

Accepted 2017 March 15. Received 2017 March 10; in original form 2017 January 18

ABSTRACT

We use globular cluster kinematics data, primarily from the SAGES Legacy Unifying Globulars and GalaxieS (SLUGGS) survey, to measure the dark matter fraction ($f_{\rm DM}$) and the average dark matter density ($\langle\rho_{\rm DM}\rangle$) within the inner 5 effective radii ($R_{\rm e}$) for 32 nearby early-type galaxies (ETGs) with stellar mass log ($M_*/{\rm M}_\odot$) ranging from 10.1 to 11.8. We compare our results with a simple galaxy model based on scaling relations as well as with cosmological hydrodynamical simulations where the dark matter profile has been modified through various physical processes. We find a high $f_{\rm DM}$ ($\geq$0.6) within 5 $R_{\rm e}$ in most of our sample, which we interpret as a signature of a late mass assembly history that is largely devoid of gas-rich major mergers. However, around log ($M_*/{\rm M}_\odot$) $\sim$ 11, there is a wide range of $f_{\rm DM}$ which may be challenging to explain with any single cosmological model. We find tentative evidence that lenticulars (S0s), unlike ellipticals, have mass distributions that are similar to spiral galaxies, with decreasing $f_{\rm DM}$ within 5 $R_{\rm e}$ as galaxy luminosity increases. However, we do not find any difference between the $\langle\rho_{\rm DM}\rangle$ of S0s and ellipticals in our sample, despite the differences in their stellar populations. We have also used $\langle\rho_{\rm DM}\rangle$ to infer the epoch of halo assembly ($z\sim2$–4). By comparing the age of their central stars with the inferred epoch of halo formation, we are able to gain more insight into their mass assembly histories. Our results suggest a fundamental difference in the dominant late-phase mass assembly channel between lenticulars and elliptical galaxies.

Key words: galaxies: evolution – galaxies: haloes – dark matter – cosmology: observations.

1 INTRODUCTION

The natural expectation within the hierarchical structure formation paradigm and Λ cold dark matter (ΛCDM) cosmology (e.g. Peebles 1982) is that dark matter (DM) haloes and their resident galaxies grow in tandem. The growth channels include mergers (major/minor, with/without gas) and gas accretion (smooth or clumpy, e.g. Genel et al. 2010; Rodriguez-Gomez et al. 2016), with galaxy assembly showing more complexities due to the baryonic processes involved (e.g. gas dissipation, star formation, feedback processes due to active galactic nuclei (AGNs) or supernovae (SNe), etc.). These baryonic processes may also alter the DM distribution, especially in the most central parts, through adiabatic halo contraction (e.g. Blumenthal et al. 1986) or halo expansion through gravitational heating from infalling gas clumps (e.g. Johansson, Naab & Ostriker 2009) or outflows linked to feedback events (e.g. Macciò et al. 2012). The implication is that the relative distributions of DM and baryons in present-day galaxies contain clues about when (epoch of formation) and how (nature of the mass assembly) they formed and how they have evolved.

Both halo and galaxy growth have been divided into two phases in the literature (e.g. Zhao et al. 2003; Oser et al. 2010; Klypin et al. 2016). At early times, when the Universe was denser, DM

★ E-mail: aalabi@swin.edu.au (ABA); dforbes@swin.edu.au (DAF)

haloes grew rapidly via frequent mergers and accretion. In parallel, gas-rich, dissipative events were very common, and the stellar cores of present-day galaxies were formed. Galaxies then grew predominantly by rapidly forming stars *in situ*, such that the DM fraction ($f_{\rm DM}$) at the centres of young galaxies is relatively low and the galaxies themselves are very compact (e.g. van Dokkum et al. 2008; Naab, Johansson & Ostriker 2009; Napolitano, Romanowsky & Tortora 2010; Remus et al. 2017). DM haloes experienced an increase in both core size and extent (core size and halo extent are usually parametrized by the scale radius ($r_{\rm s}$) and virial radius (r_{200}), respectively). Thus, the halo concentration ($c_{200} \equiv r_{200}/r_{\rm s}$) is kept fairly constant during this phase (Klypin et al. 2016). The halo concentration is directly linked to the density of the universe at the epoch when the halo formed ($c_{200} \propto (1+z_{\rm form})^{-1}$ e.g. Bullock et al. 2001; Wechsler et al. 2002) and is well described by the c_{200}–M_{200} scaling relation (e.g. Dutton et al. 2010), where M_{200} is the virial mass.

At later times ($z \leq 2$), in the two-phase paradigm, when gas-rich events become fewer, mass growth (be it baryonic or dark matter) occurs predominantly in the galaxy outskirts. The progenitors of present-day massive early-type galaxies (ETGs) increase rapidly in mass and size through a multitude of minor mergers and/or dry major mergers, thereby increasing significantly their fraction of stars formed *ex situ* (e.g. Naab et al. 2009; Pillepich et al. 2014; Rodriguez-Gomez et al. 2016; Remus et al. 2017). This is consistent with the low angular momentum content (e.g. Emsellem et al. 2011; Arnold et al. 2014; Moody et al. 2014; Raskutti, Greene & Murphy 2014; Foster et al. 2016), old central stars (e.g. Terlevich & Forbes 2002; McDermid et al. 2015) and high $f_{\rm DM}$ at large radii (e.g. Deason et al. 2012; Alabi et al. 2016) usually reported in studies of massive ETGs. The DM haloes also get bigger in size while the core sizes may grow or shrink depending on whether violent relaxation, adiabatic halo contraction or halo expansion events occur (e.g. Johansson et al. 2009; Governato et al. 2010; Klypin et al. 2016). Therefore, the observed DM density within the scale radius should reflect the epoch of halo assembly as well as imprints of how baryonic processes have altered the distribution of DM within the halo during galaxy evolution.

DM fractions at large radii, e.g. 5 effective radii ($R_{\rm e}$), are becoming increasingly available, especially in $\sim L^*$ ETGs, that is, ETGs with stellar mass (M_*) $\sim 10^{11}$ M$_\odot$ (e.g. Deason et al. 2012; Alabi et al. 2016). This is due to the use of dynamical mass tracers, such as planetary nebulae (PNe) or globular clusters (GCs), which probe further out into the galaxy halo where the light from galaxy stars is faint. At a fiducial 5 $R_{\rm e}$, which is always interior to the halo $r_{\rm s}$ (it is expected on average that, 5 $R_{\rm e} \sim 0.4 r_{\rm s}$), DM should dominate the mass profiles in ETGs. While most ETGs studied show a high DM fraction within 5 $R_{\rm e}$ (on average, $f_{\rm DM} \geq 0.6$), in agreement with theoretical predictions and an increasing trend with total galaxy stellar mass, some ETGs with $M_* \sim 10^{11}$ M$_\odot$ have been found to have surprisingly low DM content within 5 $R_{\rm e}$ (e.g. Romanowsky et al. 2003; Napolitano et al. 2005; Deason et al. 2012; Alabi et al. 2016).

Several reasons have been given in the literature for this intriguing tension between observations and simulations including the stellar initial mass function (IMF), the orbital anisotropy of the mass tracers, modification of the DM profile during mass assembly (net effect of adiabatic halo contraction and inner DM halo expansion), the nature of the DM halo profile, that is, logarithmic or Navarro-Frenk-White (NFW) or even a failure of the ΛCDM cosmology (e.g. Dekel et al. 2005; Napolitano et al. 2005, 2010, 2011; Thomas et al. 2009; Morganti et al. 2013). In Alabi et al. (2016), we suggested that these galaxies with low DM fractions could have different halo structures, that is, diffuse DM haloes. However, the exact origin of this anomaly is still unclear. Cosmological hydrodynamical simulations of ETGs where baryons have modified the present-day DM profiles have also started to report predictions for $f_{\rm DM}$ at 5 $R_{\rm e}$ (e.g. Wu et al. 2014). More recently, simulations with realistic implementation of AGN and SN feedback recipes (e.g. Vogelsberger et al. 2014; Schaye et al. 2015; Remus et al. 2017), covering the stellar mass range of ETGs in this work, that is, 10^{10}–10^{12} M$_\odot$, have been released. The time is therefore ripe to systematically compare results from observations with theoretical predictions, and thereby unravel the nature of mass distributions in ETGs within a cosmological context.

Unfortunately, the halo concentration is difficult to directly constrain in ETGs (e.g. Napolitano et al. 2005, 2009; Samurović 2014), due in part to the limited radial extent of kinematics data and the degeneracy between the halo virial mass and concentration. However, it is possible to infer the epoch of halo assembly from the average dark density within the scale radius ($\langle \rho_{\rm DM} \rangle \propto (1+z_{\rm form})^3$, where $\langle \rho_{\rm DM} \rangle$ and $z_{\rm form}$ are the average DM density and the epoch of halo assembly, respectively). Thomas et al. (2009) inferred $z_{\rm form}$ for several ETGs in the Coma cluster using $\langle \rho_{\rm DM} \rangle$ obtained from stellar kinematics within the inner 2 $R_{\rm e}$ and found that their haloes must have assembled at $z_{\rm form} \approx 2$–3.

In this work, we expand our sample of ETGs with homogeneously measured $f_{\rm DM}$ at 5 $R_{\rm e}$ in Alabi et al. (2016) from 23 to 32, using GC kinematics data mostly obtained as part of the SLUGGS[1] survey (Brodie et al. 2014). SLUGGS stands for SAGES Legacy Unifying Globulars and GalaxieS. This brings the number of $\sim L^*$ ETGs with total mass measurements within 5 $R_{\rm e}$ up to 16. We also adopt the recently published galaxy sizes, Sérsic indices and stellar mass measurements from Forbes et al. (2016) for our galaxy sample. With this larger sample, homogeneously measured galaxy parameters and the suite of cosmological simulations that are now available, we investigate the cosmological origins of the measured $f_{\rm DM}$ at large radii in ETGs. We also address the curious cases of ETGs with low DM fractions in more detail. We study the structural properties of the DM haloes within the inner 5 $R_{\rm e}$ using their average DM densities, and infer their halo assembly epochs. Lastly, we use the halo formation epoch, the age of the central stars and the DM fraction to probe the nature of mass assembly in ETGs. We pay special attention to the morphology, environment and angular momentum in this exercise.

The paper structure is as follows. In Section 2, we describe the new data we introduce in this work. In Section 3, we obtain the dynamical mass estimates and $f_{\rm DM}$ (for the newly introduced galaxies) and $\langle \rho_{\rm DM} \rangle$ (for the combined sample) and compare with cosmological hydrodynamical simulations. We also obtain DM halo properties and compare them with results from the literature. In Section 4, we discuss the diverse nature of $f_{\rm DM}$ in ETGs and the nature of their mass assembly. We summarize our results in Section 5.

2 DATA

2.1 New SLUGGS survey GC kinematics data

Here, we introduce new Keck/DEIMOS GC kinematics data for NGC 2974, NGC 4474, NGC 4459 and NGC 4697. These ETGs have log (M_*/M$_\odot$) $\sim$ 10–11. NGC 4697 was already studied in Alabi et al. (2016, hereafter Alabi+16), but the total number of GCs ($N_{\rm GC}$) with radial velocities was 20. Here, we use an improved data set for NGC 4697, with $N_{\rm GC} = 90$ and radial extent out to 4 $R_{\rm e}$.

[1] http://sluggs.swin.edu.au

The remaining newly introduced lower mass ETGs have relatively sparse data sets but always with $N_{GC} > 20$. This limit is set due to the $1/\sqrt{N_{GC}}$ nature of the uncertainty on total mass estimate such that below $N_{GC} = 20$, the uncertainty increases rapidly beyond 0.5 dex. We have therefore adopted $N_{GC} = 20$ as a sample size limit for our analysis. This is consistent with recent results from Toloba et al. (2016) and was pointed out earlier in Strader et al. (2011).

2.2 GC kinematics data from the literature

We also include six ETGs (NGC 1316, NGC 1399, NGC 4472, NGC 4594/M104, NGC 4636 and NGC 5128) from the literature, with rich GC kinematics data sets ($N_{GC} > 170$) obtained from various telescopes/instruments. For NGC 1316, we use the GC kinematics catalogue published in Richtler et al. (2014), obtained from VLT/FORS2. The data for NGC 1399 and NGC 4636 are from Schuberth et al. (2010) and Schuberth et al. (2012), respectively, also obtained from VLT/FORS2. The data for NGC 4472 are from Keck/LRIS (Côté et al. 2003). The data for NGC 4594 are from Keck/DEIMOS but with a different setup that did not use the CaT features as we have done in the SLUGGS survey (Alves-Brito et al. 2011). Finally, we also considered NGC 5128 (Centaurus A), using the GC kinematics catalogue compiled in Woodley et al. (2010). The GC kinematics data for NGC 5128 have been obtained over two decades from an array of telescopes and instruments such as CTIO/SIT, Magellan/LDSS-2, VLT/VIMOS and CTIO/HYDRA.

Unlike Keck/DEIMOS data obtained with the SLUGGS setup, where the average uncertainty on the kinematics data is $\sim$15 km s^{-1}, these externally sourced data have an average uncertainty of $\sim$50 km s^{-1}. Higher uncertainty in the kinematics data tends to wash out subtle but important details in the velocity distributions, e.g. kinematics substructures and higher velocity moments (see for example, Amorisco & Evans 2012), needed to accurately determine galaxy dynamical mass. Also, larger uncertainties on the velocities tend to bias mass estimates, especially in galaxies with low-velocity dispersions. This bias typically scales with $\Delta V_i/\sigma$, where ΔV_i and σ are the uncertainties on individual velocity measurements and the central velocity dispersion of the galaxies, respectively.

2.3 Size and stellar mass measurements

Systematic deviation of galaxies from the size–stellar mass scaling relation could create artificial tension between our DM fraction measurements and expectations from cosmological simulations. Here, we revisit and update (where necessary) the size and stellar mass measurements used in Alabi+16, as described below.

The galaxy sizes used in Alabi+16 were taken from Brodie et al. (2014), which they obtained mostly from the ATLAS^{3D} survey (Cappellari et al. 2011) based on calibrated near-IR 2MASS and optical RC3 size measurements (de Vaucouleurs et al. 1991). Such measurements, however, underestimate galaxy sizes up to a factor of $\sim$2–3 for our most massive galaxies. This naturally leads to an underestimation of the measured f_{DM} within 5 R_e. Here, we partially correct for this underestimation by adopting the recently published size measurements from Forbes et al. (2016) obtained using 3.6 μm *Spitzer* imaging data. This correction only affects the most massive galaxies in our sample, with NGC 4374 being the most severely affected, where we have now revised its R_e upwards by a factor of $\sim$3 to $\sim$12 kpc.

In Alabi+16, we obtained stellar masses for our galaxy sample from their 2MASS absolute K-band magnitude, assuming a stellar-mass-light ratio $M/L_K = 1$. While this assumption is consistent with a Kroupa/Chabrier stellar IMF, it does not account for variations in stellar age or metallicity. The implication of this assumption becomes critical in ETGs whose stellar population is dominated by younger stars, since stellar M/L_K for ETGs is known to be age-dependent. For example, at a mean stellar age of $\sim$6 Gyr, assuming solar metallicity and Padova isochrones, Röck et al. (2016) recently reported a stellar $M/L_K \sim 0.6$. This corresponds to an $\sim$0.2 dex decrease in stellar mass and an $\sim$0.1 increase in f_{DM}, which may change our earlier conclusions, especially in galaxies with low f_{DM}. One way of addressing this concern would be to apply an age-weighted correction to our previous $M/L_K = 1$ assumption. Forbes et al. (2016) applied this correction to their stellar mass estimates (they assumed a Kroupa IMF) from the 3.6 μm *Spitzer* data. We note that there is a one-to-one correspondence with the 2MASS K-band stellar mass estimates if they are also corrected for stellar age variations.

We use the homogeneously measured effective radii and total stellar mass estimates for the 27 galaxies we have in common with Forbes et al. (2016). For the remaining galaxies, we obtain their stellar mass estimates from 2MASS absolute K-band magnitudes, correcting for sky oversubtraction (Scott, Graham & Schombert 2013) and stellar age variation (Röck et al. 2016). Their effective radii are obtained from the literature studies that used 3.6 μm *Spitzer* imaging data and a similar effective radius measurement procedure as in Forbes et al. (2016). Our final sample of 32 galaxies now spans a log $(M_*/M_\odot)$ range of 10.1–11.8, with the typical uncertainty on M_* and R_e being $\sim$0.1 dex and $\sim$0.15 dex, respectively. Table 1 contains a summary of the salient properties of the galaxies used in this work.

3 METHOD AND RESULTS

3.1 Total mass estimates and DM fractions within 5 R_e

We use the tracer mass estimator (TME) of Watkins, Evans & An (2010) to obtain the total mass estimates and subsequently the DM fractions for our galaxy sample, following the implementation described in Alabi+16. We give a brief summary of the implementation below and encourage interested readers to see Alabi+16 for more details.

The TME assumes that the discrete dynamical tracers follow a power-law density distribution when de-projected and a power-law description for the gravitational potential. The pressure-supported mass within a sphere with projected radius R, $M_p(< R)$, is then

$$M_p(< R) \propto f(\alpha, \beta, \gamma) \times \left\langle V_{los}^2 R^\alpha \right\rangle, \quad (1)$$

where α and γ are the power-law slopes of the gravitational potential and the de-projected GC number density profile, respectively. β is the Binney anisotropy parameter (Binney & Tremaine 1987), assumed to be constant with radius. For each galaxy, we use equations (8) and (10) from Alabi+16 to obtain α and γ, respectively. In Alabi+16, we obtained α from the logarithmic slope of the circular velocity curves of realistic galaxies (from the cosmological simulation reported in Wu et al. 2014) at 5 R_e. We obtained γ from a compilation of GC density profiles from the literature. We found that α and γ are well approximated by

$$\alpha = (-0.46 \pm 0.06) \times \log(M_*/M_\odot) + (5.29 \pm 0.68) \quad (2)$$

and

$$\gamma = (-0.63 \pm 0.17) \times \log(M_*/M_\odot) + (9.81 \pm 1.94), \quad (3)$$

Table 1. General properties of our galaxies. Columns: (1) galaxy name: † = bonus galaxies, ‡ = SLUGGS galaxies not studied in Alabi+16; (2) distance; (3) systemic velocity; (4) central stellar velocity dispersion within 1 kpc; (5) ellipticity; (6) galaxy environment: F=field, G=group, C=cluster; (7) galaxy morphology, mostly sourced from Brodie et al. (2014), otherwise from Makarov et al. (2014), although NGC 4594 (Sombrero galaxy) is classified as an Sa, we include it in our ETG sample; (8) average luminosity-weighted age of central (1 R_e) stellar population, mostly from McDermid et al. (2015) unless otherwise noted and listed below; (9) number of GCs with kinematics data; (10) effective (half-light) radius; (11) stellar mass; (12) Sérsic n index; (10)–(12) are mostly from Forbes et al. (2016) unless otherwise noted and listed below (also see text for more details); (13) the power-law slope of the gravitational potential; (14) the power-law slope of the de–projected GC density profile; (15) normalizing factor to correct for effect of galaxy flattening on dynamical mass estimate and (16) rotation dominance parameter for the GC system [details on the derivation of columns (13)–(16) can be found in Alabi+16]. Galaxies below the horizontal line are not part of the SLUGGS survey, we have obtained their GC kinematics data from the literature.

Galaxy (NGC) (1)	Dist. (Mpc) (2)	V_{sys} ($km\,s^{-1}$) (3)	σ_{kpc} ($km\,s^{-1}$) (4)	ϵ (5)	Env. (6)	Morph. (7)	Age (Gyr) (8)	N_{GC} (9)	R_e (kpc) (10)	$\log(M_*)$ ($M_\odot$) (11)	n (12)	α (13)	γ (14)	Corr (15)	V_{rot}/σ (16)
720	26.9	1745	227	0.49	F	E	7.8[b]	69	3.80	11.27	3.8	0.106	2.71	0.92	$0.42^{+0.24}_{-0.17}$
821	23.4	1718	193	0.35	F	E	11.0	69	4.90	11.00	6.0	0.230	2.88	0.98	$0.40^{+0.20}_{-0.18}$
1023	11.1	602	183	0.63	G	S0	12.3	115	2.58	10.99	4.2	0.235	2.89	0.85	$0.65^{+0.21}_{-0.18}$
1400	26.8	558	236	0.13	G	E/S0	13.8[c]	69	3.33	11.08	5.0	0.193	2.83	1.01	$0.22^{+0.20}_{-0.15}$
1407	26.8	1779	252	0.07	G	E	12.0[c]	372	12.14	11.60	4.9	−0.046	2.50	1.01	$0.04^{+0.08}_{-0.07}$
2768	21.8	1353	206	0.57	G	E/S0	12.3	107	6.37	11.21	3.8	0.133	2.75	0.88	$0.50^{+0.15}_{-0.15}$
2974†	20.9	1887	231	0.36	F	S0	9.3	26	3.06	10.93	4.3	0.262	2.92	0.97	$0.31^{+0.12}_{-0.17}$
3115	9.4	663	248	0.66	F	S0	9.0[d]	150	1.66	10.93	4.7	0.262	2.92	0.83	$0.94^{+0.15}_{-0.16}$
3377	10.9	690	135	0.33	G	E	7.0	122	2.40	10.50	5.9	0.460	3.20	0.98	$0.23^{+0.14}_{-0.10}$
3607‡	22.2	942	229	0.13	G	S0	10.3	36	5.19	11.39	5.3	0.051	2.63	1.01	$0.18^{+0.22}_{-0.15}$
3608	22.3	1226	179	0.20	G	E	9.9	36	4.64	11.03	5.3	0.216	2.86	1.01	$0.21^{+0.26}_{-0.18}$
4278	15.6	620	228	0.09	G	E	11.8	270	2.14	10.95	6.2	0.253	2.91	1.01	$0.13^{+0.08}_{-0.07}$
4365	23.1	1243	253	0.24	G	E	13.4	251	8.71	11.51	4.9	−0.005	2.56	1.00	$0.15^{+0.10}_{-0.08}$
4374	18.5	1017	284	0.05	C	E	14.9	41	12.45	11.51	8.0	−0.005	2.56	1.01	$0.45^{+0.25}_{-0.24}$
4459†	16.0	1192	170	0.21	C	S0	7.0	36	3.75	10.98	5.4	0.239	2.89	1.01	$0.20^{+0.13}_{-0.18}$
4473	15.2	2260	189	0.43	C	E	13.1	106	2.23	10.96	5.0	0.248	2.91	0.95	$0.23^{+0.15}_{-0.11}$
4474†	15.5	1611	88	0.42	C	E/S0	10.8	23	1.50	10.23	2.8	0.584	3.37	0.95	$2.04^{+1.55}_{-1.89}$
4486	16.7	1284	307	0.16	C	E	17.7	702	7.01	11.62	5.1	−0.055	2.49	1.01	$0.14^{+0.06}_{-0.05}$
4494	16.6	1342	157	0.14	G	E	8.0	107	4.23	11.02	4.5	0.221	2.87	1.01	$0.51^{+0.15}_{-0.14}$
4526	16.4	617	233	0.76	C	S0	11.0	107	2.58	11.26	3.6	0.110	2.72	0.77	$0.61^{+0.23}_{-0.24}$
4564	15.9	1155	153	0.53	C	E	11.8	27	1.14	10.58	3.2	0.423	3.14	0.90	$1.80^{+0.51}_{-0.33}$
4649	16.5	1110	308	0.16	C	E/S0	17.7	431	6.34	11.60	4.6	−0.046	2.50	1.01	$0.34^{+0.07}_{-0.08}$
4697†	12.5	1252	180	0.32	G	E	11.3	90	5.81	11.15	5.3	0.161	2.79	0.98	$0.72^{+0.51}_{-1.31}$
5846	24.2	1712	231	0.08	G	E/S0	17.7	190	10.54	11.46	5.2	0.018	2.59	1.01	$0.08^{+0.09}_{-0.07}$
5866‡	14.9	755	163	0.58	G	S0	5.9	20	1.69	10.83	2.8	0.308	2.99	0.88	$0.16^{+1.06}_{-0.36}$
7457	12.9	844	74	0.47	F	S0	3.8	40	2.13	10.13	2.6	0.63	3.43	0.93	$1.90^{+0.53}_{-0.42}$
1316	20.8	1760	225	0.28	C	S0	4.7[e]	175[h]	8.57[n]	11.55	5.0[n]	−0.023	2.53	1.00	$0.60^{+0.10}_{-0.11}$
1399	21.2	1425	335	0.01	C	E	11.0[f]	514[i]	15.83[o]	11.50	11.1[o]	0.002	2.57	1.00	$0.09^{+0.05}_{-0.05}$
4472	16.7	981	288	0.19	C	E	17.7	263[j]	15.74[p]	11.78	6.0[p]	−0.126	2.39	1.00	$0.19^{+0.07}_{-0.08}$
4594	9.77	1024	231	0.46	G	Sa⋆	12.5[g]	232[m]	3.41	11.41	3.2	0.041	2.62	1.00	$0.13^{+0.08}_{-0.10}$
4636	14.3	930	198	0.23	C	E	13.4	386[k]	12.71[p]	11.17	5.7[p]	0.153	2.77	1.00	$0.35^{+0.08}_{-0.08}$
5128	3.8[a]	547	107	0.11	G	E/S0	−−	549[l]	2.21[n]	10.94	3.5[n]	0.258	2.92	1.00	$0.17^{+0.07}_{-0.07}$

References: *a*. Harris, Rejkuba & Harris (2010), *b*. Rembold, Pastoriza & Bruzual (2005), *c*. Spolaor et al. (2008), *d*. Norris, Sharples & Kuntschner (2006), *e*. Koleva et al. (2011), *f*. Trager et al. (2000), *g*. Sánchez-Blázquez et al. (2006), *h*. Richtler et al. (2014), *i*. Schuberth et al. (2010), *j*. Côté et al. (2003), *k*. Schuberth et al. (2012), *l*. Woodley et al. (2010), *m*. Alves-Brito et al. (2011), *n*. Sani et al. (2011), *o*. Läsker, Ferrarese & van de Ven (2014), *p*. Kormendy et al. (2009).

respectively. The most massive galaxies in our sample have $\alpha \sim 0$, that is, they are nearly isothermal, and the less massive ones are more Keplerian. Also, γ defined this way is such that $2 \leq \gamma \leq 4$, with the most massive galaxies well described by shallow GC density profiles.

Since the TME assumes that the GC system is pressure-supported, we first subtract the contribution of rotation, V_{rot}, from the line-of-sight velocity, V_{los}, before evaluating equation (1). V_{rot} is obtained by fitting an inclined-disc model to the GC kinematics data. Our total mass estimate, M_{tot}, is then evaluated as the sum of the rotationally supported mass, M_{rot}, and the pressure-supported mass, M_p. The contribution from rotation to the total mass is usually small, ∼6 per cent. We evaluate M_{tot} assuming that the orbital anisotropy of the GC system is either strongly radial, mildly tangential or

isotropic, i.e. $\beta = \pm 0.5, 0$, respectively. Since our mass estimates are largely insensitive to the choice of β (deviating by $\leq$10 per cent), we adopt $M_{\rm tot}$ obtained when $\beta = 0$, that is, the velocity distribution is isotropic. As a further test, we have also obtained $M_{\rm tot}$ assuming a more extreme velocity anisotropy of $\beta = -1$. This is motivated by recent results from dynamical studies and cosmological simulations where such anisotropies were reported (e.g. Röttgers, Naab & Oser 2014; Pota et al. 2015; Zhang et al. 2015). Even with such extreme anisotropies, the maximum deviation in total mass is less than 20 per cent, never producing a shift in DM fraction greater than 0.1 (see Appendix A1 for more details). Note that we have also applied small corrections to $M_{\rm p}$ to account for galaxy flattening and projection effects (on average, $\sim$5 per cent) and non-equilibrium conditions ($\sim$20 per cent when kinematics substructures are identified in the GC system).

For the newly introduced galaxies and at the lower M_* end, the average fractional uncertainty on $M_{\rm tot}$ is 0.4 dex. At the high M_* end of our sample, there is no significant difference between the fractional uncertainties on $M_{\rm tot}$ for galaxies with externally sourced kinematics data, compared to galaxies with Keck/DEIMOS data. We are unable to identify any kinematics substructures that may be in the GC systems of these newly introduced galaxies. This is due to the large uncertainties on the individual radial velocities. Since our kinematics data extend well beyond 5 $R_{\rm e}$ for most galaxies in our sample, we also obtain $M_{\rm tot}$ enclosed within the maximum radial extent, $R_{\rm max}$, of our data. We obtain the DM fraction, $f_{\rm DM}$, as $1 - M_*(<R)/M_{\rm tot}(<R)$ where we assume that all of the baryonic mass within R in our galaxies is stellar in nature. We describe the total stellar mass within 5 $R_{\rm e}$ with de-projected Sérsic profiles, using the Sérsic indices from Table 1. Table 2 contains a summary of the total masses and DM fractions enclosed within 5 $R_{\rm e}$ and $R_{\rm max}$.

For the galaxies originally studied in Alabi+16, we compare results in Fig. 1 to see how the newly adopted sizes and stellar masses affect both parameters of interest. We remark that while these new galaxy parameters result in changes to the total mass and DM fraction estimates within 5 $R_{\rm e}$ on a galaxy by galaxy basis, their overall distributions, which we will present shortly, for our galaxy sample remain unchanged. In particular, at the high M_* end, galaxies are now more massive within the 5 $R_{\rm e}$ aperture and a few $\sim L^*$ galaxies also have slightly lowered DM fractions compared to Alabi+16.

Fig. 2 shows the $f_{\rm DM}$ versus M_* for our galaxy sample, assuming $\beta = 0$ and a Kroupa IMF. For most galaxies in our combined sample, the DM content already dominates the mass budget at 5 $R_{\rm e}$ with the DM domination increasing as we probe beyond 5 $R_{\rm e}$ into the outer haloes. There is a wide diversity in the measured $f_{\rm DM}$ within 5 $R_{\rm e}$, ranging from 0.1to0.9, generally increasing with galaxy stellar mass, with some $\log(M_*/{\rm M}_\odot) \sim 11$ galaxies having very low $f_{\rm DM}$, that is, $\leq$0.4, less than what a simple galaxy model (SGM) predicts. This trend persists for a variety of stellar M/L assumptions, assumed slope of the gravitational potential and orbital anisotropies. The large spread in $f_{\rm DM}$ is driven exclusively by $\log(M_*/{\rm M}_\odot) \sim 11$ ETGs. The updated list of galaxies with $f_{\rm DM}$ within 5 $R_{\rm e}$ lower than the prediction from our SGM now consist of NGC 720, NGC 2974, NGC 3607, NGC 4494, NGC 4526 and NGC 5866. A complete inventory of our galaxy sample shows that 2 out of 5 field galaxies, 3 out of 15 group galaxies and 1 out of 12 cluster galaxies have low DM fractions. This is the same as 2 out of 16 ellipticals, 4 out of 10 lenticulars and none of the 6 galaxies with ambiguous morphological classification having low DM fractions.

The results we have obtained for NGC 2974 may appear to be at odds with that reported in the H I study of Weijmans et al. (2008) where they obtained a DM fraction of 0.55 within 5 $R_{\rm e}$ and a $M_{\rm tot}(<5R_{\rm e}) = 2.7 \times 10^{11}$ M$_\odot$ for their maximal disc model, compared to our values (for the isotropic orbit case) of 0.08 ± 0.45 and $M_{\rm tot}(<5R_{\rm e}) = 0.8 \pm 0.4 \times 10^{11}$ M$_\odot$. The stellar mass and galaxy size used in the two studies are comparable. If we assume $\alpha = 0$ (i.e. the isothermal case as suggested by their flat rotation curve), we would derive a somewhat higher DM fraction of 0.15. The main limitation on our DM fraction measurement for NGC 2974 is likely the limited sample size of 26 GCs; this results in a relatively large error. Despite different data sets and modelling assumptions in both studies, our low DM fraction is consistent within $\sim 1\sigma$ of the Weijmans et al. value. Therefore, these intriguing results of very low DM fractions would need confirmation by future studies to rule out that it is not the poor number statistics that is driving these results, although we also find $f_{\rm DM} \sim 0.8$ in NGC 3608 with $M_* \sim 10^{11}$ M$_\odot$ and similarly sparse GC kinematics data.

To properly understand our observed $f_{\rm DM}$, we compare our results with expectations from simple galaxy models and the cosmological hydrodynamical simulations reported in Wu et al. (2014, hereafter Wu+14) and in Remus et al. (2017, hereafter Remus+17). The simple galaxy model, labelled SGM1, (details of which are presented in Alabi+16) does not account directly for processes that are believed to alter the distribution of baryons and non-baryons in present-day ETGs during their evolution. It takes as input the $R_{\rm e}$–M_*, M_*–M_{200} and M_{200}–c_{200} scaling relations from the literature, adopts the *Planck* cosmology and predicts the $f_{\rm DM}$ and the $M_{\rm tot}$ within 5 $R_{\rm e}$ for a given M_*. On the other hand, the mass distribution is explicitly modified in the cosmological simulation of Wu+14 via dissipative and/or non-dissipative processes during galaxy assembly. However, they did not include feedback models from AGN and/or SN winds in their simulations. The immediate effect of this is that their galaxies contain more baryons relative to DM when compared to conventional M_*–M_{200} scaling relations for ETGs. If we allow for a factor of 2–3 excess stellar mass at any defined M_{200} in our SGM1 model, we adequately predict the $f_{\rm DM}$ reported in Wu+14, as shown in Fig. 2. The predicted $f_{\rm DM}$ from our SGM1 is then reduced by $\sim$0.1 at all galaxy stellar mass. The cosmological simulation of Remus+17 is an improvement on Wu+14 in that they have included a feedback model that accounts for AGN and SN winds effects. However, at low M_*, their galaxies are larger than the expectations from conventional $R_{\rm e}$–M_* scaling relations for ETGs (e.g. Lange et al. 2015). This probably indicates AGN feedback that is too strong in their lower stellar mass regime. Lastly, we construct a variant of our SGM1 where we use the galaxy sizes, stellar masses and Sérsic indices listed in Table 1 and compare the predicted DM fractions with what we have measured within 5 $R_{\rm e}$. We show the comparison in Fig. 3 as a function of galaxy stellar mass. We also show this simple galaxy model (labelled SGM2) in Fig. 2 where we have used a double-power law fit to the galaxy sizes and stellar masses in Table 1, and show that it is consistent (within 1σ) with the dark matter fractions predicted by SGM1. This galaxy model captures the shape of our measured dark matter fractions better than SGM1.

3.2 Average DM density

We obtain the average enclosed DM density, $\langle \rho_{\rm DM} \rangle$, within a sphere with radius R, as in Thomas et al. (2009) using

$$\langle \rho_{\rm DM} \rangle = \frac{M_{\rm DM}(<R)}{(4\pi/3)R^3}, \quad (4)$$

Table 2. Summary of mass estimates and DM fractions assuming different anisotropy. The results shown here have been obtained using the TME and a stellar M/L that accounts for stellar age variation. $M_{\rm p}$ is the pressure-supported mass and has been corrected for the effect of galaxy flattening. $M_{\rm rot}$ is the rotationally supported mass. $M_{\rm tot}$ is the total mass after correcting for galaxy flattening, rotation in the GC system and the presence of kinematics substructures. $f_{\rm DM}$ is the DM fraction. We list masses enclosed within spheres of radius 5 $R_{\rm e}$ and $R_{\rm max}$, the maximum galactocentric radius where we have GC kinematics data. Note that the kinematics data for NGC 4374, NGC 4472, NGC 4636 and NGC 4697 do not extend out to 5 $R_{\rm e}$.

Galaxy (NGC)	β	$M_{\rm rot}(<5R_{\rm e})$ ($10^{10}{\rm M}_\odot$)	$M_{\rm p}(<5R_{\rm e})$ ($10^{11}{\rm M}_\odot$)	$M_{\rm tot}(<5R_{\rm e})$ ($10^{11}{\rm M}_\odot$)	$f_{\rm DM}(<5R_{\rm e})$	$R_{\rm max}$ ($R_{\rm e}$)	$M_{\rm rot}(<R_{\rm max})$ ($10^{10}{\rm M}_\odot$)	$M_{\rm p}(<R_{\rm max})$ ($10^{11}{\rm M}_\odot$)	$M_{\rm tot}(<R_{\rm max})$ ($10^{11}{\rm M}_\odot$)	$f_{\rm DM}(<R_{\rm max})$
720	0	1.7 ± 0.3	2.4 ± 0.6	2.6 ± 0.5	0.36 ± 0.20	22.91	7.6 ± 1.6	11.4 ± 2.2	12.2 ± 2.0	0.85 ± 0.04
	0.5		2.4 ± 0.6	2.6 ± 0.5	0.34 ± 0.21			11.1 ± 2.2	11.9 ± 2.0	0.84 ± 0.04
	−0.5		2.5 ± 0.6	2.6 ± 0.6	0.37 ± 0.18			11.6 ± 2.3	12.4 ± 2.2	0.85 ± 0.04
821	0	2.1 ± 0.4	4.3 ± 0.8	4.5 ± 0.8	0.81 ± 0.05	8.06	3.4 ± 0.6	5.6 ± 1.0	5.9 ± 1.0	0.85 ± 0.04
	0.5		4.4 ± 0.8	4.6 ± 0.9	0.82 ± 0.05			5.8 ± 1.0	6.1 ± 1.0	0.85 ± 0.04
	−0.5		4.2 ± 0.8	4.4 ± 0.8	0.81 ± 0.05			5.5 ± 1.0	5.8 ± 1.0	0.85 ± 0.04
1023	0	2.4 ± 0.4	1.4 ± 0.3	1.6 ± 0.2	0.47 ± 0.12	16.15	7.7 ± 1.4	3.2 ± 0.6	3.9 ± 0.5	0.76 ± 0.05
	0.5		1.5 ± 0.3	1.7 ± 0.2	0.49 ± 0.12			3.3 ± 0.6	4.1 ± 0.5	0.76 ± 0.05
	−0.5		1.4 ± 0.3	1.6 ± 0.2	0.46 ± 0.13			3.1 ± 0.5	3.9 ± 0.5	0.75 ± 0.05
1400	0	0.3 ± 0.1	2.2 ± 0.5	2.2 ± 0.6	0.54 ± 0.21	22.55	1.6 ± 0.6	7.1 ± 1.3	7.2 ± 1.3	0.84 ± 0.04
	0.5		2.2 ± 0.6	2.3 ± 0.6	0.54 ± 0.2			7.2 ± 1.3	7.4 ± 1.3	0.84 ± 0.04
	−0.5		2.2 ± 0.5	2.2 ± 0.5	0.53 ± 0.17			7.0 ± 1.3	7.1 ± 1.2	0.83 ± 0.04
1407	0	0.1 ± 0.1	18.6 ± 1.5	18.6 ± 1.5	0.82 ± 0.04	9.54	0.2 ± 0.1	36.4 ± 2.7	36.4 ± 2.7	0.90 ± 0.02
	0.5		16.5 ± 1.4	16.5 ± 1.4	0.79 ± 0.04			32.2 ± 2.4	32.2 ± 2.4	0.88 ± 0.02
	−0.5		19.7 ± 1.6	19.7 ± 1.7	0.83 ± 0.03			38.5 ± 2.8	38.5 ± 2.7	0.90 ± 0.02
2768	0	4.3 ± 0.4	6.3 ± 1.1	6.8 ± 0.9	0.78 ± 0.05	11.36	9.8 ± 0.9	12.0 ± 1.9	13.0 ± 1.7	0.88 ± 0.02
	0.5		6.3 ± 1.0	6.7 ± 0.9	0.78 ± 0.05			11.9 ± 1.9	12.9 ± 1.7	0.88 ± 0.03
	−0.5		6.4 ± 1.1	6.8 ± 0.9	0.79 ± 0.05			12.1 ± 1.9	13.1 ± 1.7	0.88 ± 0.02
2974	0	0.5 ± 0.1	0.8 ± 0.4	0.8 ± 0.4	0.08 ± 0.45	10.69	1.0 ± 0.3	4.9 ± 1.5	5.0 ± 1.5	0.84 ± 0.09
	0.5		0.8 ± 0.4	0.9 ± 0.4	0.12 ± 0.44			5.1 ± 1.6	5.2 ± 1.6	0.84 ± 0.11
	−0.5		0.8 ± 0.4	0.8 ± 0.4	0.06 ± 0.48			4.8 ± 1.5	4.9 ± 1.4	0.83 ± 0.09
3115	0	3.4 ± 0.6	1.7 ± 0.3	2.1 ± 0.3	0.64 ± 0.08	17.6	11.8 ± 2.1	4.4 ± 0.6	5.6 ± 0.6	0.85 ± 0.03
	0.5		1.8 ± 0.4	2.2 ± 0.3	0.65 ± 0.08			4.6 ± 0.7	5.8 ± 0.6	0.86 ± 0.03
	−0.5		1.7 ± 0.3	2.0 ± 0.3	0.63 ± 0.09			4.3 ± 0.6	5.5 ± 0.6	0.85 ± 0.03
3377	0	0.1 ± 0.1	0.7 ± 0.1	0.7 ± 0.1	0.62 ± 0.09	11.37	0.3 ± 0.1	1.3 ± 0.2	1.3 ± 0.2	0.77 ± 0.05
	0.5		0.8 ± 0.1	0.8 ± 0.1	0.66 ± 0.09			1.4 ± 0.2	1.5 ± 0.2	0.80 ± 0.04
	−0.5		0.6 ± 0.1	0.7 ± 0.1	0.60 ± 0.10			1.2 ± 0.2	1.2 ± 0.2	0.76 ± 0.05
3607	0	0.4 ± 0.1	2.4 ± 0.7	2.5 ± 0.7	0.16 ± 0.44	16.76	1.3 ± 0.5	10.2 ± 2.4	10.3 ± 2.4	0.77 ± 0.09
	0.5		2.3 ± 0.6	2.4 ± 0.6	0.11 ± 0.38			9.6 ± 2.3	9.7 ± 2.2	0.75 ± 0.08
	−0.5		2.5 ± 0.7	2.6 ± 0.6	0.18 ± 0.38			10.4 ± 2.5	10.5 ± 2.6	0.77 ± 0.24
3608	0	0.5 ± 0.2	3.9 ± 1.1	4.0 ± 1.2	0.77 ± 0.19	6.82	0.7 ± 0.3	4.4 ± 1.2	4.5 ± 1.2	0.78 ± 0.12
	0.5		4.1 ± 1.2	4.1 ± 1.2	0.78 ± 0.11			4.5 ± 1.2	4.6 ± 1.2	0.79 ± 0.1
	−0.5		3.9 ± 1.1	3.9 ± 1.1	0.77 ± 0.2			4.3 ± 1.2	4.4 ± 1.2	0.78 ± 0.12
4278	0	0.1 ± 0.1	2.6 ± 0.3	2.7 ± 0.4	0.72 ± 0.07	16.81	0.5 ± 0.2	6.5 ± 0.6	6.6 ± 0.6	0.87 ± 0.02
	0.5		2.8 ± 0.4	2.8 ± 0.4	0.73 ± 0.06			6.8 ± 0.6	6.9 ± 0.6	0.88 ± 0.02
	−0.5		2.6 ± 0.3	2.6 ± 0.3	0.72 ± 0.07			6.3 ± 0.6	6.4 ± 0.5	0.87 ± 0.02
4365	0	1.5 ± 0.2	16.5 ± 1.6	16.6 ± 1.6	0.83 ± 0.03	8.79	2.6 ± 0.3	29.7 ± 2.6	30.0 ± 2.6	0.90 ± 0.02
	0.5		15.1 ± 1.4	15.2 ± 1.5	0.82 ± 0.04			27.1 ± 2.4	27.4 ± 2.4	0.89 ± 0.02
	−0.5		17.3 ± 1.6	17.4 ± 1.6	0.84 ± 0.03			31.0 ± 2.8	31.3 ± 2.7	0.90 ± 0.02
4374	0	16.1 ± 1.4	20.9 ± 4.8	22.5 ± 4.9	0.89 ± 0.04	3.51	–	–	–	–
	0.5		19.1 ± 4.4	20.7 ± 4.4	0.88 ± 0.04		–	–	–	–
	−0.5		21.8 ± 5.0	23.4 ± 5.3	0.90 ± 0.04		–	–	–	–
4459	0	0.2 ± 0.1	2.1 ± 0.6	2.2 ± 0.6	0.62 ± 0.32	7.27	0.3 ± 0.1	2.6 ± 0.7	2.7 ± 0.7	0.68 ± 0.14
	0.5		2.2 ± 0.6	2.2 ± 0.6	0.64 ± 0.17			2.7 ± 0.7	2.8 ± 0.7	0.69 ± 0.13
	−0.5		2.1 ± 0.6	2.1 ± 0.6	0.62 ± 0.39			2.6 ± 0.7	2.6 ± 0.7	0.67 ± 0.13
4473	0	0.2 ± 0.1	1.6 ± 0.3	1.6 ± 0.3	0.51 ± 0.15	15.51	0.8 ± 0.4	3.6 ± 0.5	3.7 ± 0.5	0.76 ± 0.05
	0.5		1.7 ± 0.3	1.7 ± 0.3	0.53 ± 0.12			3.7 ± 0.6	3.8 ± 0.5	0.77 ± 0.05
	−0.5		1.5 ± 0.3	1.6 ± 0.3	0.50 ± 0.14			3.5 ± 0.5	3.6 ± 0.5	0.75 ± 0.05
4474	0	1.2 ± 1.2	0.4 ± 0.2	0.6 ± 0.2	0.71 ± 0.42	17.18	4.2 ± 4.6	0.9 ± 0.3	1.3 ± 0.6	0.87 ± 0.38
	0.5		0.5 ± 0.2	0.6 ± 0.3	0.75 ± 0.41			1.0 ± 0.4	1.4 ± 0.6	0.88 ± 0.44
	−0.5		0.4 ± 0.2	0.5 ± 0.2	0.70 ± 0.45			0.8 ± 0.3	1.2 ± 0.6	0.86 ± 0.44
4486	0	1.7 ± 0.2	25.5 ± 1.8	25.7 ± 1.9	0.86 ± 0.03	28.55	9.8 ± 1.0	148.0 ± 8.4	149.0 ± 8.4	0.97 ± 0.01
	0.5		22.5 ± 1.6	22.7 ± 1.6	0.84 ± 0.03			130.0 ± 7.3	131.0 ± 7.6	0.97 ± 0.01
	−0.5		27.1 ± 1.9	27.3 ± 1.9	0.87 ± 0.03			157.0 ± 8.8	158.0 ± 9.2	0.97 ± 0.01
4494	0	1.3 ± 0.1	1.4 ± 0.2	1.5 ± 0.2	0.4 ± 0.14	7.95	2.0 ± 0.2	1.9 ± 0.3	2.1 ± 0.3	0.53 ± 0.11
	0.5		1.4 ± 0.2	1.6 ± 0.2	0.41 ± 0.13			1.9 ± 0.3	2.2 ± 0.3	0.54 ± 0.10
	−0.5		1.4 ± 0.2	1.5 ± 0.2	0.39 ± 0.14			1.9 ± 0.3	2.1 ± 0.3	0.52 ± 0.10
4526	0	2.1 ± 0.6	2.7 ± 0.8	2.9 ± 0.6	0.43 ± 0.18	16.75	7.0 ± 2.1	6.5 ± 1.3	7.2 ± 1.1	0.75 ± 0.05
	0.5		2.6 ± 0.8	2.8 ± 0.6	0.41 ± 0.20			6.4 ± 1.3	7.1 ± 1.0	0.74 ± 0.06
	−0.5		2.7 ± 0.8	2.9 ± 0.6	0.43 ± 0.19			6.6 ± 1.4	7.3 ± 1.1	0.75 ± 0.06

Table 2 – *continued*

Galaxy (NGC)	β	$M_{\rm rot}(<5R_{\rm e})$ ($10^{10}{\rm M}_\odot$)	$M_{\rm p}(<5R_{\rm e})$ ($10^{11}{\rm M}_\odot$)	$M_{\rm tot}(<5R_{\rm e})$ ($10^{11}{\rm M}_\odot$)	$f_{\rm DM}(<5R_{\rm e})$	$R_{\rm max}$ ($R_{\rm e}$)	$M_{\rm rot}(<R_{\rm max})$ ($10^{10}{\rm M}_\odot$)	$M_{\rm p}(<R_{\rm max})$ ($10^{11}{\rm M}_\odot$)	$M_{\rm tot}(<R_{\rm max})$ ($10^{11}{\rm M}_\odot$)	$f_{\rm DM}(<R_{\rm max})$
4564	0	1.8 ± 0.4	0.7 ± 0.2	0.9 ± 0.2	0.59 ± 0.22	11.25	4.0 ± 0.9	0.9 ± 0.3	1.3 ± 0.3	0.71 ± 0.09
	0.5		0.8 ± 0.3	0.9 ± 0.3	0.62 ± 0.15			1.0 ± 0.3	1.4 ± 0.3	0.73 ± 0.09
	−0.5		0.6 ± 0.2	0.8 ± 0.2	0.57 ± 0.2			0.9 ± 0.3	1.3 ± 0.3	0.70 ± 0.08
4649	0	4.6 ± 0.3	12.9 ± 1.0	13.4 ± 1.0	0.74 ± 0.05	20.2	18.6 ± 1.3	53.9 ± 3.8	55.8 ± 3.8	0.93 ± 0.01
	0.5		11.4 ± 0.9	11.9 ± 0.9	0.71 ± 0.05			47.8 ± 3.3	49.7 ± 3.4	0.92 ± 0.01
	−0.5		13.7 ± 1.1	14.2 ± 1.1	0.75 ± 0.05			57.0 ± 4.0	58.9 ± 3.9	0.93 ± 0.01
4697	0	3.1 ± 0.2	3.6 ± 0.6	3.9 ± 0.6	0.7 ± 0.07	4.0	–	–	–	–
	0.5		3.6 ± 0.6	3.9 ± 0.6	0.7 ± 0.07		–	–	–	–
	−0.5		3.5 ± 0.6	3.9 ± 0.5	0.7 ± 0.07		–	–	–	–
5846	0	0.4 ± 0.1	18.4 ± 1.9	18.4 ± 1.9	0.87 ± 0.03	8.99	0.8 ± 0.2	32.5 ± 3.3	32.6 ± 3.3	0.92 ± 0.02
	0.5		17.0 ± 1.8	17.0 ± 1.8	0.86 ± 0.03			30.1 ± 3.0	30.2 ± 3.1	0.91 ± 0.02
	−0.5		19.0 ± 2.0	19.0 ± 2.0	0.87 ± 0.03			33.7 ± 3.4	33.8 ± 3.4	0.92 ± 0.02
5866	0	0.1 ± 0.1	1.0 ± 0.5	1.0 ± 0.4	0.34 ± 0.45	8.85	0.1 ± 0.6	1.2 ± 0.5	1.2 ± 0.4	0.44 ± 0.39
	0.5		1.0 ± 0.5	1.0 ± 0.4	0.38 ± 0.45			1.3 ± 0.5	1.3 ± 0.5	0.48 ± 0.42
	−0.5		0.9 ± 0.5	0.9 ± 0.4	0.32 ± 0.44			1.1 ± 0.5	1.2 ± 0.4	0.42 ± 0.38
7457	0	1.8 ± 0.2	0.9 ± 0.3	1.1 ± 0.2	0.88 ± 0.04	6.61	2.4 ± 0.3	0.9 ± 0.3	1.2 ± 0.2	0.89 ± 0.04
	0.5		1.1 ± 0.3	1.2 ± 0.3	0.90 ± 0.04			1.1 ± 0.3	1.3 ± 0.3	0.90 ± 0.03
	−0.5		0.8 ± 0.2	1.0 ± 0.2	0.87 ± 0.04			0.8 ± 0.2	1.1 ± 0.2	0.88 ± 0.04
1316	0	12.0 ± 0.4	14.6 ± 2.1	15.8 ± 2.0	0.81 ± 0.04	9.45	22.6 ± 0.8	29.3 ± 3.6	31.6 ± 3.4	0.89 ± 0.02
	0.5		13.2 ± 1.9	14.4 ± 1.9	0.79 ± 0.05			26.4 ± 3.2	28.7 ± 3.4	0.88 ± 0.02
	−0.5		15.4 ± 2.2	16.6 ± 2.1	0.82 ± 0.04			30.8 ± 3.7	33.1 ± 3.6	0.90 ± 0.02
1399	0	0.2 ± 0.1	40.8 ± 2.7	40.8 ± 2.6	0.94 ± 0.01	6.06	0.2 ± 0.1	49.4 ± 3.2	49.4 ± 3.1	0.95 ± 0.01
	0.5		37.4 ± 2.5	37.4 ± 2.4	0.94 ± 0.01			45.3 ± 2.9	45.3 ± 3.0	0.95 ± 0.01
	−0.5		42.5 ± 2.8	42.5 ± 2.9	0.94 ± 0.01			51.5 ± 3.3	51.5 ± 3.4	0.95 ± 0.01
4472	0	0.2 ± 0.1	29.6 ± 2.8	29.6 ± 2.8	0.85 ± 0.04	3.12	–	–	–	–
	0.5		24.6 ± 2.3	24.6 ± 2.4	0.82 ± 0.04		–	–	–	–
	−0.5		32.2 ± 3.1	32.2 ± 3.0	0.86 ± 0.03		–	–	–	–
4594	0	0.3 ± 0.1	5.6 ± 0.6	5.7 ± 0.6	0.58 ± 0.08	10.0	0.6 ± 0.3	9.9 ± 0.9	9.9 ± 0.9	0.75 ± 0.05
	0.5		5.3 ± 0.5	5.3 ± 0.6	0.56 ± 0.09			9.3 ± 0.9	9.4 ± 0.9	0.73 ± 0.05
	−0.5		5.8 ± 0.6	5.8 ± 0.6	0.59 ± 0.08			10.2 ± 1.0	10.3 ± 1.0	0.75 ± 0.05
4636	0	1.0 ± 0.1	9.5 ± 0.7	9.6 ± 0.7	0.88 ± 0.02	3.48	–	–	–	–
	0.5		9.5 ± 0.7	9.6 ± 0.7	0.88 ± 0.03		–	–	–	–
	−0.5		9.5 ± 0.7	9.6 ± 0.7	0.88 ± 0.02		–	–	–	–
5128	0	0.1 ± 0.1	1.7 ± 0.2	1.7 ± 0.2	0.53 ± 0.09	21.73	0.6 ± 0.3	7.4 ± 0.5	7.5 ± 0.5	0.88 ± 0.02
	0.5		1.7 ± 0.2	1.7 ± 0.2	0.54 ± 0.09			7.6 ± 0.5	7.7 ± 0.5	0.89 ± 0.02
	−0.5		1.6 ± 0.2	1.6 ± 0.1	0.52 ± 0.09			7.3 ± 0.5	7.4 ± 0.5	0.88 ± 0.02

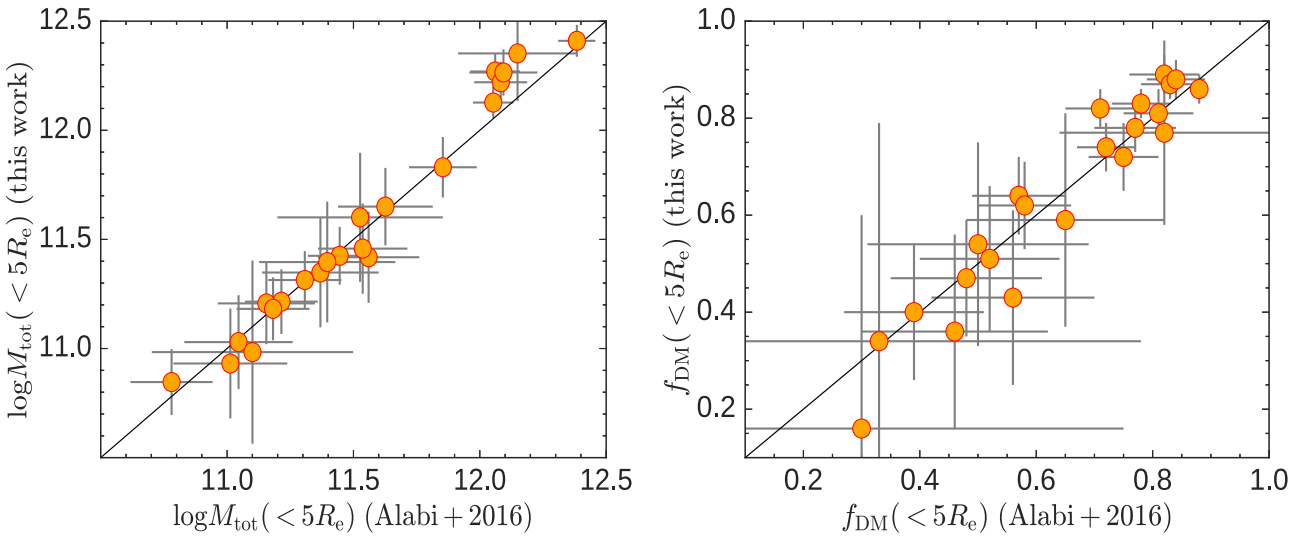

Figure 1. Comparison of total mass estimates (left-hand panel) and DM fractions (right-hand panel) obtained using different galaxy sizes and stellar masses (see text for details). Note that we have excluded NGC 4697 from these plots due to the additional change to its kinematics data.

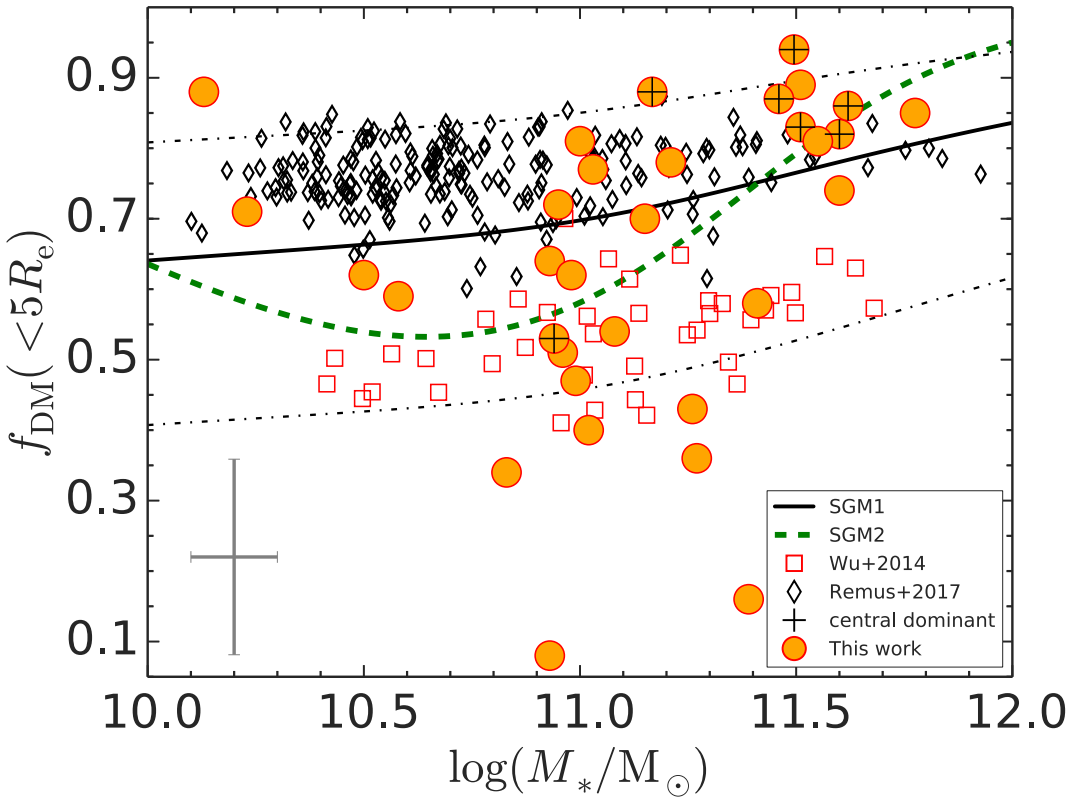

Figure 2. Measured dark matter fraction, $f_{\rm DM}$, within 5 effective radii ($R_{\rm e}$) versus the total stellar mass, M_* assuming $\beta = 0$, i.e. isotropic velocity distribution. The solid black line (SGM1) shows the predicted dark matter fraction within 5 $R_{\rm e}$ assuming *Planck* cosmology and Kroupa IMF for a simple galaxy model based on scaling relations for early-type galaxies. The dot-dashed black lines are the 1σ scatter in the predicted dark matter fractions from the adopted $R_{\rm e} - M_*$ relation. We also show results from the cosmological hydrodynamical simulations reported in Wu et al. (2014) and Remus et al. (2017) for comparison. The dashed green line (SGM2) is the predicted dark matter fraction from a simple galaxy model using a fit to galaxy sizes and stellar masses in Table 1. The orange-coloured circles and the lower left representative errorbar are for our galaxy sample. Galaxies with $\log(M_*/{\rm M}_\odot) \sim 11$ have a larger spread in their measured $f_{\rm DM}$, with a few of them having $f_{\rm DM}$ lower than predicted by any cosmological model. At any stellar mass, central dominant galaxies (marked with crosses) mostly have higher $f_{\rm DM}$.

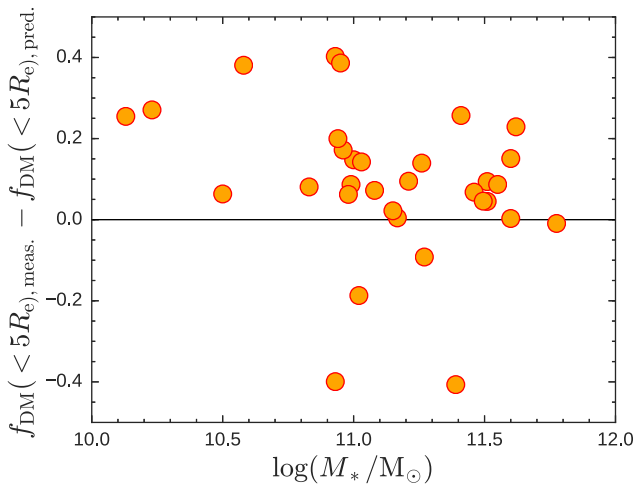

Figure 3. Residuals between observed and predicted DM fractions, assuming a *Planck* cosmology and using galaxy sizes, stellar masses and Sérsic indices from Table 1 in the simple galaxy model, that is, SGM2.

where $M_{\rm DM}$ is the enclosed DM mass, evaluated as $M_{\rm tot}(<R) - M_*(<R)$. Again we have followed the approach used in Alabi+16, where we assume that all the baryonic matter within our 5 $R_{\rm e}$ aperture is in the stellar component.

Fig. 4 shows the log $\langle\rho_{\rm DM}\rangle$ within 5 $R_{\rm e}$ for our galaxy sample. We also show similar data from Thomas et al. (2009), Wegner et al. (2012) and Corsini et al. (2017), but obtained within 2 $R_{\rm e}$ for several ETGs in the Coma cluster, the nearby Abell 262 cluster and low-density environments, respectively. The offset between these literature results and our measurements is due to the difference between the apertures used. The general trend, regardless of the adopted aperture, is for $\langle\rho_{\rm DM}\rangle$ to decrease with M_*, with an enhanced scatter around $\log(M_*/{\rm M}_\odot)\sim11$. A wide range of average DM densities is possible at any stellar mass, in agreement with theory, where galaxies are expected to have diverse mass assembly histories at any stellar mass. We do not see any difference between the mean average densities for the lenticulars or ellipticals in our galaxy sample, neither do we see any significant trend with galaxy environment. The increasing trend earlier observed in $f_{\rm DM}$ as a function of mass is now reversed when $\langle\rho_{\rm DM}\rangle$ is compared with M_*. This is due to the steep increase of $R_{\rm e}$ with M_*, such that in the more massive galaxies, our fiducial radius now encloses more DM within a much more increased

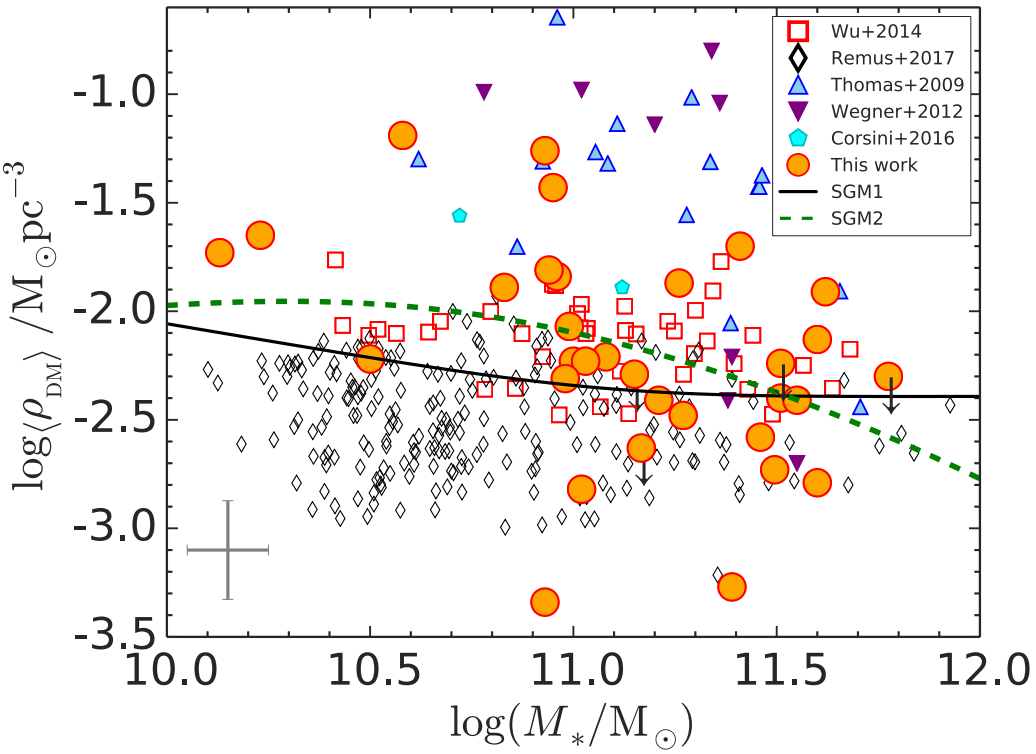

Figure 4. Average DM density within 5 $R_{\rm e}$, $\langle\rho_{\rm DM}\rangle$, versus the stellar mass for our galaxy sample. Results from Thomas et al. (2009) for ETGs in the Coma cluster, Wegner et al. (2012) for eight galaxies in the nearby, but poor Abell 262 cluster and Corsini et al. (2017) for two galaxies in low-density environments within 2 $R_{\rm e}$ are also shown. The offset from our data is due to differences in the apertures used. Galaxies with sub-5 $R_{\rm e}$ kinematics data are marked with downward-pointing arrows. The solid and dashed lines are the predicted average dark matter densities within 5 $R_{\rm e}$ from our simple galaxy models, that is, SGM1 and SGM2, respectively. We have also included results from the cosmological simulations of Wu+14 and Remus+17. Average DM density within 5 $R_{\rm e}$ (as well as within any other aperture) decreases mildly with total stellar mass, with a larger scatter around $\log(M_*/{\rm M}_\odot)\sim11$.

volume, hence the lowered density. The increased offset at the low stellar mass end between our measurements and the predictions from Remus+17 is due to the relatively large galaxies produced in their simulations.

3.3 Inferring DM halo properties from dynamical measurements

Next, we turn to one of the main questions we wish to address in this work, that is, given dynamical mass measurements at some fiducial radii (in our case, 5 $R_{\rm e}$), which are smaller than the typical scale radii in DM haloes, can we *reliably* infer the structural properties of these haloes, that is, M_{200} (virial mass), c_{200} (halo concentration) and $z_{\rm form}$ (the halo assembly epoch)?

DM haloes can generally be described by Navarro–Frenk–White (NFW) profiles (Navarro, Frenk & White 1996) where the average enclosed DM density, $\langle\rho_{\rm DM}\rangle$, can be expressed as

$$\langle\rho_{\rm DM}\rangle\,(<R) = \frac{200}{x^3}\frac{\ln(1+cx)-cx/(cx+1)}{\ln(1+c)-c/(c+1)}\rho_{\rm crit}, \qquad (5)$$

where $x \equiv R/r_{200}$ and $c \equiv c_{200} \equiv r_{200}/r_{\rm s}$ (r_{200} is the virial radius and c_{200} is the NFW DM halo concentration), with $r_{\rm s}$ being the scale radius of the DM halo, corresponding to the radius where the logarithmic slope of the DM density profile is -2. The virial overdensity, Δ_{200}, is 200 times the critical density, $\rho_{\rm crit} = 1.37\times10^2\ {\rm M}_\odot\ {\rm kpc}^{-3}$. Since the RHS of equation (5) has two unknown quantities (c_{200} and r_{200}), it cannot be solved uniquely without some extra assumptions. We solve equation (5) using the mock galaxies in our SGM1 with the following steps:

(i) For mock galaxies with M_* identical to our galaxy sample, obtain galaxy sizes using the $R_{\rm e}$–M_* relation from Lange et al. (2015).

(ii) Use the $R_{\rm e}$–n relation from Graham (2013) to obtain Sérsic indices (Sérsic 1968) for each mock galaxy.

(iii) Calculate the total M_* enclosed within 5 $R_{\rm e}$ with the de–projected Sérsic mass profile (Terzić & Graham 2005).

(iv) Calculate M_{200} for each mock galaxy using the M_*–M_{200} relation for ETGs from Dutton et al. (2010), which assumes a *Planck* cosmology. Note that r_{200} follows directly from M_{200}.

(v) Calculate the total DM mass, $M_{\rm DM}$ enclosed within 5 $R_{\rm e}$, from the cumulative NFW DM only profile.

(vi) Calculate the ratio of M_{200} to $M_{\rm tot}$ within 5 $R_{\rm e}$ for each mock galaxy.

(vii) Assume that for any M_*, given the ratio of M_{200} to $M_{\rm tot}$ within 5$R_{\rm e}$ obtained from our mock galaxies, we can extrapolate our measured $M_{\rm tot}$ within 5 $R_{\rm e}$ to obtain the corresponding M_{200}.

As a sanity test, we have compared the ratio of our measured $M_{\rm tot}$ within 5 $R_{\rm e}$ to the extrapolated M_{200} for our galaxy sample with that from Wu+14. The scaling ratios we have used are consistent with those inferred from their simulations, bearing in mind that they have overproduced stars by factors of 2–3. Armed with the *extrapolated* M_{200}, which we transform to r_{200} using $M_{200} = 4\pi\Delta_{200}\rho_{\rm crit}{r_{200}}^3/3$, we then numerically solve the non-linear equation (5) and obtain c_{200} given our measured $\langle\rho_{\rm DM}\rangle$ within 5 $R_{\rm e}$. We have used Monte Carlo methods to propagate uncertainties from our mass measurements and the scaling relations at every stage of this analysis. From our results, c_{200} increases steeply as $\langle\rho_{\rm DM}\rangle$ increases, such that an

Table 3. Summary of inferred halo parameters. Columns: (1) galaxy name; (2) average DM density within 5 R_e; (3) halo mass; (4) halo concentration; (5) halo assembly epoch (we have set the halo assembly epoch of galaxies with invalid z_{form} to 0.1; these are all galaxies with very low DM fractions); (6) redshift corresponding to the mean luminosity-weighted stellar age from Table 1. For galaxies with mean stellar ages comparable to or older than the age of the universe, we have set their corresponding z_{stars} to a lower limit of 10.

Galaxy (NGC)	log M_{200} ($M_\odot$)	log $\langle\rho_{DM}\rangle$ ($M_\odot pc^{-3}$)	c_{200}	z_{form}	z_{stars}
720	12.83 ± 0.38	-2.48 ± 0.65	3.0 ± 2.0	0.6 ± 0.8	1.0
821	12.99 ± 0.29	-2.23 ± 0.22	6.4 ± 1.5	2.3 ± 0.6	2.4
1023	12.56 ± 0.28	-2.07 ± 0.37	6.2 ± 2.2	2.3 ± 0.9	4.1
1400	12.71 ± 0.36	-2.21 ± 0.49	5.4 ± 2.6	1.9 ± 1.1	>10
1407	13.82 ± 0.40	-2.79 ± 0.11	2.3 ± 0.3	0.5 ± 0.3	3.5
2768	13.22 ± 0.33	-2.41 ± 0.18	4.7 ± 0.9	1.6 ± 0.5	4.1
2974	12.25 ± 0.55	-3.34 ± 6.34	0.01 ± 6.6	0.1	1.4
3115	12.65 ± 0.25	-1.26 ± 0.23	17.9 ± 3.7	6.9 ± 1.4	1.3
3377	12.19 ± 0.20	-2.22 ± 0.27	5.7 ± 1.6	2.0 ± 0.7	0.8
3607	12.85 ± 0.45	-3.27 ± 1.98	0.2 ± 2.0	0.1	1.9
3608	12.95 ± 0.38	-2.23 ± 0.39	6.2 ± 2.5	2.2 ± 1.0	1.7
4278	12.76 ± 0.26	-1.43 ± 0.20	15.7 ± 2.9	6.1 ± 1.1	3.2
4365	13.73 ± 0.39	-2.40 ± 0.12	4.4 ± 0.5	1.4 ± 0.3	10.0
4374	13.86 ± 0.43	-2.24 ± 0.25	5.6 ± 1.4	2.0 ± 0.7	10.0
4459	12.67 ± 0.37	-2.31 ± 0.47	5.1 ± 2.5	1.7 ± 1.0	0.8
4473	12.55 ± 0.29	-1.84 ± 0.40	8.5 ± 3.2	3.2 ± 1.3	7.5
4474	12.13 ± 0.46	-1.65 ± 0.63	11.6 ± 7.2	4.5 ± 2.5	2.2
4486	13.97 ± 0.40	-1.91 ± 0.09	7.8 ± 0.7	2.9 ± 0.3	>10
4494	12.53 ± 0.28	-2.82 ± 0.45	1.9 ± 1.1	0.1	1.0
4526	12.87 ± 0.38	-1.87 ± 0.54	7.2 ± 3.5	2.7 ± 1.4	2.4
4564	12.27 ± 0.29	-1.19 ± 0.44	18.6 ± 7.3	7.2 ± 2.7	3.2
4649	13.68 ± 0.40	-2.13 ± 0.11	5.7 ± 0.6	2.0 ± 0.3	>10
4697	12.96 ± 0.32	-2.29 ± 0.23	5.4 ± 1.3	1.9 ± 0.6	2.6
5846	13.75 ± 0.38	-2.58 ± 0.13	3.5 ± 0.5	0.9 ± 0.3	>10
5866	12.31 ± 0.46	-1.89 ± 1.26	6.9 ± 6.3	2.6 ± 2.0	0.6
7457	12.43 ± 0.24	-1.73 ± 0.24	11.4 ± 2.7	4.4 ± 1.1	0.3
1316	13.73 ± 0.41	-2.41 ± 0.17	4.1 ± 0.7	1.3 ± 0.4	0.4
1399	14.11 ± 0.38	-2.73 ± 0.07	2.9 ± 0.2	0.5 ± 0.2	2.4
4472	14.11 ± 0.42	-2.30 ± 0.12	4.5 ± 0.5	1.4 ± 0.3	>10
4594	12.75 ± 0.14	-1.70 ± 0.21	15.3 ± 3.4	5.9 ± 1.3	4.6
4636	13.36 ± 0.30	-2.63 ± 0.09	3.7 ± 0.4	1.0 ± 0.2	>10
5128	12.56 ± 0.24	-1.81 ± 0.24	8.9 ± 2.0	3.4 ± 0.8	–

order of magnitude increase in $\langle\rho_{DM}\rangle$ corresponds to a factor of ∼3 increase in c_{200}.

The final step in estimating the epoch of halo assembly is to transform our inferred halo concentrations into halo assembly epochs. Tools that efficiently do this transformation are now readily available. For each estimated c_{200}, we use the COMMAH package from Correa et al. (2015), which is based on NFW DM profiles, to obtain the corresponding halo formation redshift, z_{form}, given the halo concentration, c_{200}, while adopting the *Planck* cosmology. This NFW parametrization matches well with our earlier preference to describe our DM haloes with NFW profiles, rather than with cored logarithmic DM haloes or other alternate parametrizations and thus enables us to calibrate our DM densities directly into halo assembly epochs. In the COMMAH package, z_{form} is the epoch when the virial mass of any progenitor halo is equivalent to the mass within its present-day scale radius. Table 3 contains a summary of the inferred halo properties for our galaxy sample. From Table 3, low $\langle\rho_{DM}\rangle$ corresponds to more recently formed haloes and vice versa. Galaxies with $c_{200} \leq 2$ (NGC 4494, NGC 2974 and NGC 3607) have invalid z_{form} from the COMMAH package and for these, we fix their halo formation epoch at $z_{form} \sim 0.1$. These are all galaxies with low f_{DM} within 5 R_e.

Table 4. Comparison of halo properties with literature results. Columns: (1) galaxy name; (2) halo mass; (3) halo concentration; (4) *corrected* halo mass from the literature; (5) *corrected* halo concentration from the literature; (6) virial overdensity, halo mass and concentration (where necessary, we have obtained corresponding halo mass and concentration at virial overdensity of 200).

Galaxy (NGC)	logM_{200} ($M_\odot$)	c_{200}	logM_{200} ($M_\odot$)	c_{200}	Notes Δ_x, logM_x, c_x
	This work		Literature		
720	12.83	3.0	12.77	14.15	101.6, 12.82, 18.50[a]
821	12.99	6.4	17.52	1.73	101, 17.68, 2.45[b]
821			14.31	1.77	101, 14.46, 2.50[c]
1400	12.71	5.4	11.92	3.98	101, 12.02, 5.38[d]
1407	13.82	2.3	13.23	7.77	101, 13.3, 10.30[e]
			13.78	6.85	101, 13.85, 9.10[f]
			12.99	5.63	101, 13.07, 7.53[d]
			13.57	12.11	200, 13.57, 12.11[g]
			13.34	18.59	200, 13.34, 18.60[h]
			12.96	13.68	101.7, 13.02, 17.88[a]
2768	13.22	4.7	11.69	4.72	101, 11.78, 6.35[d]
3115	12.65	17.9	12.08	13.79	101, 12.14, 18.07[d]
3377	12.19	5.7	11.28	5.25	101, 11.36, 7.03[d]
4278	12.76	15.7	11.71	13.23	101, 11.77, 17.35[d]
4365	13.73	4.4	12.53	11.01	101, 12.59, 14.48[d]
4374	13.86	5.6	13.14	10.97	178, 13.15, 11.50[i]
			13.32	5.59	100, 13.4, 7.50[j]
4486	13.97	7.8	13.93	6.98	101, 14.0, 9.27[k]
			12.61	12.78	101, 12.67, 16.77[d]
			14.67	3.21	101, 14.78, 4.38[l]
			13.90	3.88	101, 14.0, 5.25[m]
			13.95	3.83	101, 14.05, 5.19[n]
4494	12.53	1.9	11.97	6.23	101, 12.05, 8.30[c]
			12.02	4.32	101, 12.11, 5.82[d]
4649	13.68	5.7	13.49	15.94	101.5, 13.54, 20.80[a]
			13.47	5.94	Δ not stated[o]
4697	12.96	5.4	12.66	4.53	101, 12.75, 6.10[c]
5846	13.75	3.5	13.16	6.00	101, 13.24, 8.00[p]
			12.76	11.40	101, 12.82, 14.99[d]
			13.10	8.90	200, 13.1, 8.90[q]
1316	13.73	4.1	13.37	6.10	Δ not stated[w]
1399	14.11	2.9	13.31	13.57	101, 13.26, 11.00[r]
			12.89	10.20	101, 12.95, 13.44[s]
4472	14.11	4.5	13.45	9.93	101.4, 13.51, 13.07[a]
			13.94	–	200, *eqn.*16[t]
4636	13.36	3.7	13.13	7.37	101, 13.07, 5.90[u]
			12.99	20.09	200, 12.99, 20.10[v]

References: [a]Buote et al. (2007), [b]Forestell & Gebhardt (2010), [c]Napolitano et al. (2009), [d]Samurović (2014), [e]Pota et al. (2015), [f]Romanowsky et al. (2009), [g]Su et al. (2014), [h]Zhang et al. (2007), [i]Zhu et al. (2014), [j]Napolitano et al. (2011), [k]Oldham & Auger (2016), [l]McLaughlin (1999), [m]Strader et al. (2011), [n]Murphy, Gebhardt & Adams (2011), [o]Shen & Gebhardt (2010), [p]Napolitano et al. (2014), [q]Zhu et al. (2016), [r]Richtler et al. (2014), [s]Schuberth et al. (2010), [t]Samurović (2016), [u]Côté et al. (2003), [v]Schuberth et al. (2012), [w]Johnson et al. (2009).

3.4 Comparison of halo properties with literature studies

Some of the galaxies in our sample have published c_{200} and M_{200} results in the literature from various studies. These studies are based on data from extended PNe and/or GC kinematics (sometimes supplemented with stellar kinematics data) and X-ray studies, with different modelling techniques. We compile these results in Table 4

and where a virial overdensity other than Δ_{200} has been used in the literature, we rescale the results using the conversion relations from Hu & Kravtsov (2003). Note that while our M_{200} and literature M_{200} are generally consistent, our c_{200} values are generally lower than literature results and by construction, are more consistent with expectations from the M_{200}–c_{200} relations. The implication of adopting the c_{200} reported in the literature for our galaxy sample is that on average, their haloes are already in place at $z_{\rm form} \sim 5$, whereas we find a mean $z_{\rm form} \sim 3$. This is due to the extra constraint from the stellar mass–halo mass relation that we have placed on M_{200}. A similar approach was used in Auger et al. (2013) where the M_{200}–c_{200} relation was used as a conditional prior on c_{200}. This eased the tension between theoretical expectations and results often reported in the literature (e.g. Napolitano et al. 2011; Samurović 2014, 2016).

4 DISCUSSION

Present-day galaxies are expected to have experienced different merger (major and/or minor) and gas accretion (smooth and/or clumpy) histories of DM and baryons. It is also expected that signatures of these varied assembly histories should be reflected in their mass distributions and halo structural properties. In this work, we have obtained DM fractions and average DM densities within the inner 5 $R_{\rm e}$ for our sample of ETGs. We interpret the diversity we observe in these parameters as a reflection of their different mass assembly histories. We also use these homogeneously obtained mass measurements to infer the assembly epochs of their haloes as well as their structural parameters.

4.1 Origin of the diverse DM fractions within 5 $R_{\rm e}$ in ETGs

From our results above, it appears that galaxies with $f_{\rm DM} \sim 0.7$, in particular, the central dominant types, are well described by the simulation from Remus+17, while those with $f_{\rm DM} \sim 0.5$ appear to be better described by Wu+14. A few galaxies have inferred $f_{\rm DM}$ well below the results from both cosmological simulations. Again, we note that in the simulations of Wu+14 and Remus+17, the DM distributions have been modified from the standard NFW-like profiles through baryon–DM interactions. Also, Remus+17 included feedback from AGN and SN.

During the late phase of the mass assembly (i.e. $z \leq 2$) in these simulations, growth is dominated by dry mergers (major/minor) and happens predominantly in the outer haloes. Due to this mostly non-dissipative growth in size and mass, our fiducial 5 $R_{\rm e}$ now encloses more DM relative to stars compared to their high-redshift progenitors. At any given stellar mass, ETGs with higher DM fractions have experienced a late phase mass assembly that is increasingly dominated by dry mergers. However, the present-day mass distribution, parametrized by the $f_{\rm DM}$, also depends on the extent to which the inner DM halo has been modified by baryonic processes during the mass build-up of the galaxies, as well as the initial conditions set by the density of the universe during the initial halo collapse. We explore this in more details below and note that none of the cosmological simulations (nor any that we are aware of in the literature) produce galaxies with $f_{\rm DM}$ within 5 $R_{\rm e}$ as low as we have measured in some of our ETGs.

While the simple galaxy model (SGM1) clearly captures the mean DM fraction at any stellar mass, its use in properly understanding the origin of the diversity in our measured $f_{\rm DM}$ is hampered by the large scatter around the mean $f_{\rm DM}$. This scatter is from the combined uncertainties from the input scaling relations (i.e. $R_{\rm e}$–M_*, M_*–M_{200} and M_{200}–c_{200}). There is an ∼0.25 dex scatter in the $R_{\rm e}$–M_*, an ∼0.2 dex scatter in the M_*–M_{200} and an ∼0.11 dex scatter in the M_{200}–c_{200} scaling relations, with the scatter in the $R_{\rm e}$–M_* being the most critical. Deviations of individual galaxies from the $R_{\rm e}$–M_* scaling relation produce an asymmetrical bias towards lowered $f_{\rm DM}$ (see Fig. 3, where we measure higher $f_{\rm DM}$ than predicted for most of our galaxies), resulting in the wide range of plausible DM fractions. However, these deviations do not explain why the galaxies with low DM fractions preferentially have $\log(M_*/{\rm M}_\odot)\sim11$. SGM2, the simple galaxy model we constructed based on a fit to the sizes and stellar masses in Table 1, could potentially help shed more light on this since it captures better the general trend in our measured $f_{\rm DM}$. However, to properly address this issue, one would need to study more galaxies with $\log(M_*/{\rm M}_\odot) \leq 10.5$ to rule out any artificial bias from our sample selection.

The low $f_{\rm DM}$ ETGs, all with $\log(M_*/{\rm M}_\odot)\sim11$, have very low average DM densities within 5 $R_{\rm e}$, and from our preceding analysis, they have unrealistic halo assembly epochs, appearing to be incompatible with the *Planck* cosmology. However, they are *normal* ETGs in that they have $R_{\rm e}$ and M_* that are compatible with the $R_{\rm e}$–M_* galaxy scaling relation. It is remarkable that $\log(M_*/{\rm M}_\odot)\sim11$ corresponds to the sharp upturn in the $R_{\rm e}$–M_* scaling relation and the knee in the M_*–M_{200} scaling relation. At this stellar mass (also at all redshifts), galaxies are most efficient at converting baryons into stars e.g. Rodriguez-Gomez et al. (2016), such that a low DM fraction should then be a natural expectation. Above $\log(M_*/{\rm M}_\odot)\sim11$, galaxy haloes are too massive for gas to cool and form stars while below this mass they are not massive enough to hold on to their gas. This makes $\log(M_*/{\rm M}_\odot)\sim11$ ETGs interesting as one should be able to observe the effects of extended star formation history on galaxy evolution through their mass distributions.

From our SGM1, we find that haloes of $\log(M_*/{\rm M}_\odot)\sim11$ ETGs have significantly lower $r_{\rm s}/R_{\rm e}$ (ratio of DM halo scale radius to galaxy size) compared to ETGs at other stellar masses (see Appendix A2). A simple experiment with a mock $\log(M_*/{\rm M}_\odot)\sim11$ galaxy, where we increase $r_{\rm s}$ by a factor of 3 to reflect a more diffuse DM halo, sufficiently reduces the $f_{\rm DM}$ by a factor of 2, that is, from ∼0.6 to ∼0.3. This implies that any mechanism that can produce *normal* galaxies in diffuse DM haloes should be able to explain the low DM fractions we have observed in these galaxies. The physical processes to achieve this include halo expansion through dynamical friction from infalling stellar clumps (Johansson et al. 2009) or feedback-induced DM outflows (Governato et al. 2010). The modified DM profile would then be non-NFW and as such our analysis here which assumes an NFW-like profile would be inadequate.

The low DM fractions could also be due to the preferential tidal stripping of DM haloes relative to their stars (e.g. Smith et al. 2016) from gravitational interactions with their neighbours. If this were to be the case, then one would expect to find signatures of depletion in the GC population, especially in the galaxy outskirts, since they are more radially extended than the starlight. However, we find evidence to the contrary from their GC subpopulations (e.g. Forbes et al. 2016), where for example, the low DM fraction galaxy NGC 4494 still retains a high fraction of blue GCs relative to its entire GC system in the galaxy outskirts (the blue GCs usually dominate the GC system in galaxy outer haloes).

Alternatively, their low DM fractions could mean that their DM haloes are poorly described by NFW DM profiles. This suggests the need for an alternate halo description, e.g. using logarithmic DM haloes (Thomas et al. 2009; Morganti et al. 2013; Alabi+16). Interestingly, logarithmic DM haloes are characterized by shallow central DM densities with a maximal stellar contribution (e.g. Gentile et al. 2004; Napolitano et al. 2011), reinforcing our earlier

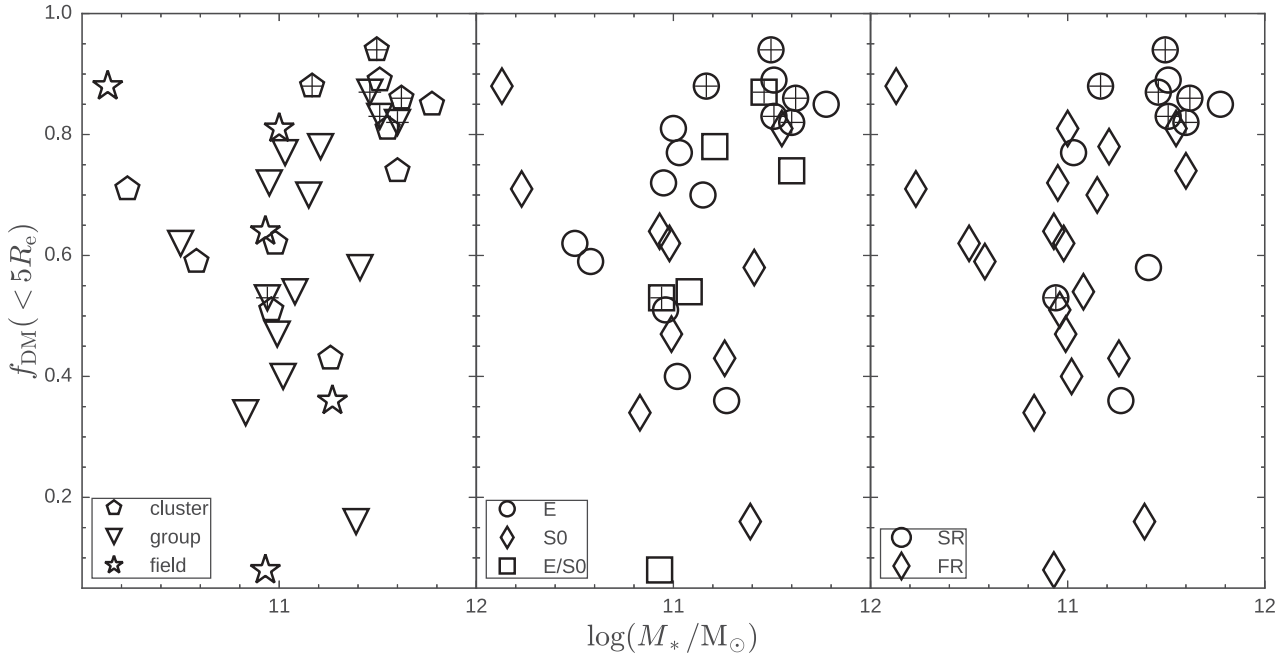

Figure 5. DM fraction versus total stellar mass, highlighting different galaxy environments in the left-hand panel, galaxy morphologies in the middle panel and galaxy central kinematics in the right-hand panel (SR = slow rotators; FR = fast rotators). Centrally dominant galaxies have been marked with black crosses and they mostly have high DM fractions. As a function of morphology, DM fraction appears to increase with galaxy stellar mass in ellipticals while lenticulars show a noisy, somewhat decreasing trend with mass and a lower median $f_{\rm DM}$ compared to elliptical galaxies. The decreasing trend with stellar mass in lenticulars from the middle panel is not seen in the fast rotators in the right-hand panel.

inference. The presence of self-interacting DM in haloes can also lower the central DM densities (e.g. Rocha et al. 2013; Di Cintio et al. 2017) by making the core radius larger, but it would be challenging to separate its effects from those purely driven by feedback outflows, especially in $\log(M_*/{\rm M}_\odot)\sim11$ galaxies.

4.2 DM fractions and correlation with galaxy properties

We revisit the issue of correlation between the DM fractions within 5 $R_{\rm e}$ for our enlarged sample and some of their galaxy properties. We briefly summarize the interesting trends below and show the trends in Fig. 5. The Spearman rank correlations between the DM fractions and galaxy properties are all statistically insignificant and generally weak, mainly due to the large scatter due to the $\sim10^{11}$ ${\rm M}_\odot$ galaxies.

First, trends as a function of environment are generally weak. The only stand-out trend we find as a function of galaxy environment is that central dominant ETGs mostly have high DM fractions with low DM fraction ETGs preferentially residing in less-dense environments. Second, we find that S0s are observed to have lower median DM fractions compared to ellipticals, and probably show a hint of an opposite trend in their DM fractions with stellar mass compared to ellipticals. This is similar to results reported for spirals in the literature (Persic, Salucci & Ashman 1993; Dutton et al. 2011; Courteau & Dutton 2015), where the most massive spirals have the lowest central DM fractions. This trend was also tentatively identified in the S0s studied in Tortora et al. (2009), although, due to their spherical modelling technique, they claimed that the trend may not be real. Interestingly, this trend is lost when our sample is classified according to their central kinematics, that is, fast or slow rotators (using results from the ATLAS$^{\rm 3D}$; Cappellari et al. 2013).

If this dichotomy in the large-scale mass distribution between S0s and ellipticals is real, it implies that S0s are akin to spirals, more than ellipticals. Disc-dominated galaxies would then have a global mass distribution where the DM fraction decreases with stellar mass, at least within 1 $R_{\rm e}$ (e.g. Courteau & Dutton 2015), and out to large radii. This agrees with results from Cappellari et al. (2015) where they found that central fast-rotators and discy lenticular galaxies have similar mass distributions out to 4 $R_{\rm e}$. A larger and more complete sample of ETGs probed to large radii would be needed to confirm if indeed this dichotomy is real or not, as well as predictions of the large-scale mass distributions from cosmological simulations that produce S0s and ellipticals.

4.3 When did the haloes of ETGs form?

We summarize the inferred halo assembly epochs for our galaxy sample in Fig. 6, showing how they vary with galaxy total stellar mass and size. Lower mass galaxies are associated with haloes that assembled earlier; $z_{\rm form}\sim4$, while the more massive galaxies have haloes that assembled later, at $z_{\rm form}\sim2$. Likewise, more compact galaxies are associated with haloes that assembled earlier, and vice versa. These results are consistent with hierarchical growth of structures such that smaller objects virialize early in gas-rich events, with today's massive galaxies undergoing a more extended halo build-up. The Spearman rank correlation between $z_{\rm form}$ and stellar mass is $\sim-$ 0.5 and only marginally significant; however, if we remove the galaxies with very low DM fractions, that is, NGC 2974, NGC 3607 and NGC 4494, the correlation becomes statistically significant, that is, p-val <0.005. The correlation between $z_{\rm form}$ and size, on the other hand, is stronger ($\sim-$ 0.7) and statistically significant (p-val <0.005) regardless of whether we exclude the three galaxies with low DM fractions or not.

In Fig. 7, we compare $z_{\rm form}$ with that of the central stellar populations (obtained from the *luminosity-weighted* ages within their central 1 $R_{\rm e}$; McDermid et al. 2015) for our galaxies. We adopt the

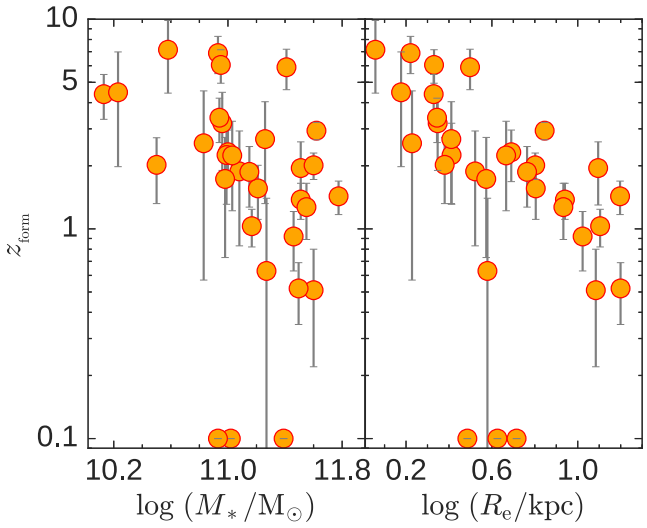

Figure 6. Halo assembly epoch as a function of total stellar mass (left-hand panel) and galaxy size (right-hand panel). The three galaxies with unrealistic halo assembly epochs are shown at $z_{\rm form} \sim 0.1$. Lower mass and/or smaller galaxies reside in haloes that assembled earlier than their more massive and larger counterparts, in agreement with the hierarchical structure growth. However, at any stellar mass or galaxy size, there exists a large spread in the inferred halo formation epoch. Also note the correlation between the average DM density from Fig. 4 and the halo assembly epoch, such that galaxies with high DM densities assemble their haloes early.

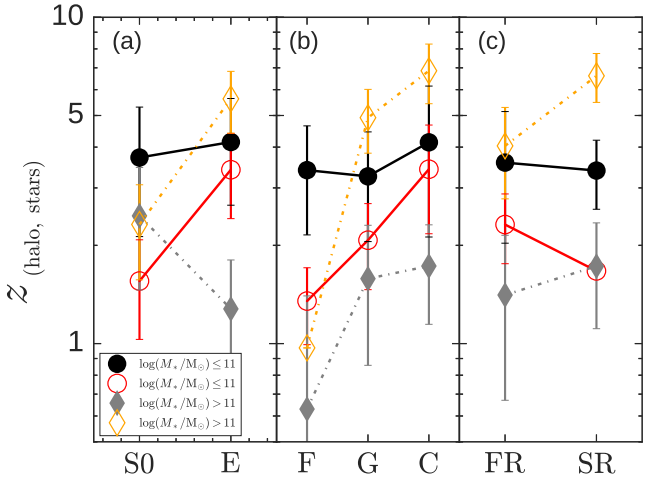

Figure 7. Summary plot showing the mean halo assembly epoch for our galaxy sample, in low ($\log(M_*/{\rm M}_\odot) \leq 11$, circles and solid lines) and high ($\log(M_*/{\rm M}_\odot) > 11$, diamonds and dash–dotted lines) stellar mass bins. Filled symbols correspond to halo assembly epochs while open symbols show the mean formation epoch that corresponds the luminosity-weighted ages of the central stars in our sample. Panel *a* shows the mean assembly epoch according to galaxy morphology (E=elliptical, S0=lenticular). Note that we have excluded all galaxies with ambiguous morphological classification from this analysis. Panel *b* shows mean assembly epoch as a function of galaxy environment (F=field, G=group, C=cluster) and panel *c* shows the mean assembly epoch as a function of central galaxy kinematics (FR=fast central rotator, SR=slow central rotator). The error bars are the standard deviations about the mean. While there are large spreads about the mean, massive ellipticals have haloes that assemble relatively late compared to lenticulars or low-mass ellipticals. We also find that massive ellipticals in the field have haloes that assemble very late in agreement with predictions from the semi-analytic galaxy formation models of De Lucia & Blaizot (2007).

cosmological parameters of a flat universe from the Planck Collaboration XVI (2014), that is, $H_0 = 67.8$ km s^{-1} Mpc^{-1}, $\Omega_{\rm M} = 0.307$ and use the ASTROPY.COSMOLOGY package to convert the ages to formation epochs. This exercise enables us to infer the nature of the late mass assembly in our sample of ETGs, that is, dissipational or non–dissipational, assuming that late gas-rich merger events are always accompanied by central star formation. For some of our galaxies, the stellar age from the literature is comparable to, or more than, the age of the universe (∼13.8 Gyr). In such cases, we adopt a fixed upper limit of ≥13.3 Gyr ($z_{\rm stars} \geq 10$).

Due to the strong correlation of $z_{\rm form}$ with stellar mass, we make our comparisons after binning our galaxies by their stellar masses. Bearing in mind our modest sample size, we consider two stellar mass bins, that is, $\log(M_*/{\rm M}_\odot) \leq 11$ and $\log(M_*/{\rm M}_\odot) > 11$ and make the comparison with respect to galaxy morphology, environment and central kinematics. From Fig. 7, massive ellipticals have haloes that assembled late, that is, $z_{\rm form} < 2$, compared to massive lenticulars, whose haloes assembled earlier ($z_{\rm form} \sim 4$). The halo assembly epoch of low-mass ellipticals is not significantly different from that of lenticulars, in that their haloes also assembled early ($z_{\rm form} \sim 3$). The late halo assembly in the field for the most massive galaxies is mainly driven by the galaxies with very low DM fractions. This is in line with results from semi-analytic models (e.g. De Lucia & Blaizot 2007) of galaxy formation where galaxies in low-density environments are expected to be associated with haloes that assembled later than those in cluster environments (see also Corsini et al. 2017, where they arrived at a similar conclusion based on their low-density environment dynamical study). However, we only find this agreement in our most massive field galaxies, that is, $\log(M_*/{\rm M}_\odot) > 11$. If on the other hand, we disregard the stellar mass binning, halo assembly epoch then has no correlation with galaxy environment (see Appendix A3 for a version of Fig. 7 but without stellar mass binning). Haloes associated with more massive slow or fast rotating galaxies also have late assembly epochs compared to their low-mass counterparts. There is however a strong trend in the central stellar age as a function of galaxy morphology, environment and central kinematics in both stellar mass bins, where the central stars are usually in place at earlier times relative to the halo in bulge-dominated systems. The only exception to this is in low-mass, slow rotators that form their central stars relatively late, that is, $z_{\rm form} \sim 2$. Our results therefore suggests a dichotomy between the late mass evolution of the bulge-dominated ellipticals and the discy lenticulars.

This dichotomy, together with our earlier results, where at any stellar mass, more massive and centrally dominant ETGs have higher DM fractions and lower average DM densities within 5 $R_{\rm e}$, form a consistent picture when considered in the context of the two-phase galaxy formation paradigm for massive ETGs (e.g. Naab et al. 2009; Oser et al. 2010; Forbes et al. 2016). Dry mergers, after the early dissipational phase, increase the inner DM fractions in massive ETGs since they do not bring a significant amount baryons to the galaxy centres but rather lead to a net outward transfer of angular momentum via dynamical friction. They also reduce the inner average DM densities since they make the galaxies larger. These findings therefore rule out wet-major merger or gas-rich accretion events as the predominant channel for the late mass build-up of massive ETGs.

5 CONCLUSIONS

We have measured the DM fraction and average DM density within 5 $R_{\rm e}$ in a sample of 32 ETGs using their GC kinematics. We compared

our DM fractions with predictions from cosmological simulations. We also used our measured dynamical parameters to infer the epochs of assembly of our ETG haloes, assuming DM haloes are well described by NFW profiles. We briefly summarize our results here.

(i) ETGs have a wide range of DM fractions within 5 R_e, ranging from 0.1 to 0.9, typically increasing with galaxy stellar mass, and largely independent of the galaxy's environment. We find that a high DM fraction is consistent with a late ($z \leq 2$) mass assembly that is dominated by dissipationless mergers.

(ii) We find that ETGs with low DM fractions within 5 R_e are typically those with $\log(M_*/M_\odot) \sim 11$ and diffuse DM haloes. We associate their low DM fractions with a mass assembly likely dominated by halo expansion.

(iii) By comparing our results with predictions from a suite of cosmological simulations, we are able to show that modifications of the mass distribution due to physical processes during mass assembly are important in understanding the distribution of DM fraction in present-day ETGs.

(iv) ETGs reside in haloes that assembled, on average, $z_{form} \sim 2$–3. The $\sim L^*$ ETGs have haloes that assembled earlier ($z \sim 4$) than their more massive counterparts that assembled later ($z \sim 2$). We find that massive galaxies, that is, $\log(M_*/M_\odot) > 11$, in the field environment have haloes that form late, in agreement with predictions from semi-analytic galaxy formation models.

(v) S0s and ellipticals reside in DM haloes with similar structural properties and assembly epochs. However, we find hints that there may be a dichotomy in their mass distributions at large radii, with S0s showing signs of a decreasing DM fraction with increasing galaxy stellar mass, unlike ellipticals. We attribute this to a fundamental difference in their dominant late-phase mass assembly channel.

ACKNOWLEDGEMENTS

We wish to thank Rhea Remus and Alan Duffy for interesting conversations and their assistance with simulation results and software packages. We thank the anonymous referee for comments and suggestions that have been helpful.

The data presented herein were obtained at the W. M. Keck Observatory, which is operated as a scientific partnership among the California Institute of Technology, the University of California and the National Aeronautics and Space Administration. The Observatory was made possible by the generous financial support of the W. M. Keck Foundation. We also wish to recognize and acknowledge the very significant cultural role and reverence that the summit of Maunakea has always had within the indigenous Hawaiian community. The analysis pipeline used to reduce the DEIMOS data was developed at UC Berkeley with support from NSF grant AST-0071048. JB acknowledges support from NSF grant AST-1616598. AJR was supported by NSF grant AST-1616710. DAF thanks the ARC for financial support via DP 130100388. JS acknowledges support from the Packard Foundation. We acknowledge the use of the HYPERLEDA data base (http://leda.univ-lyon1.fr), ASTROPY (Astropy Collaboration 2013) and TOPCAT (Taylor 2005).

REFERENCES

Alabi A. B. et al., 2016, MNRAS, 460, 3838 (Alabi+16)
Alves-Brito A., Hau G. K. T., Forbes D. A., Spitler L. R., Strader J., Brodie J. P., Rhode K. L., 2011, MNRAS, 417, 1823
Amorisco N. C., Evans N. W., 2012, MNRAS, 424, 1899
Arnold J. A. et al., 2014, ApJ, 791, 80
Astropy Collaboration, 2013, A&A, 558, A33
Auger M. W., Budzynski J. M., Belokurov V., Koposov S. E., McCarthy I. G., 2013, MNRAS, 436, 503
Binney J., Tremaine S., 1987, Galactic Dynamics. Princeton Univ. Press, Princeton, NJ
Blumenthal G. R., Faber S. M., Flores R., Primack J. R., 1986, ApJ, 301, 27
Brodie J. P. et al., 2014, ApJ, 796, 52
Bryan S. E., Kay S. T., Duffy A. R., Schaye J., Dalla Vecchia C., Booth C. M., 2013, MNRAS, 429, 3316
Bullock J. S., Kolatt T. S., Sigad Y., Somerville R. S., Kravtsov A. V., Klypin A. A., Primack J. R., Dekel A., 2001, MNRAS, 321, 559
Buote D. A., Gastaldello F., Humphrey P. J., Zappacosta L., Bullock J. S., Brighenti F., Mathews W. G., 2007, ApJ, 664, 123
Cappellari M. et al., 2011, MNRAS, 413, 813
Cappellari M. et al., 2013, MNRAS, 432, 1709
Cappellari M. et al., 2015, ApJ, 804, L21
Correa C. A., Wyithe J. S. B., Schaye J., Duffy A. R., 2015, MNRAS, 450, 1521
Corsini E. M., Wegner G. A., Thomas J., Saglia R. P., Bender R., 2017, MNRAS, 466, 974
Côté P., McLaughlin D. E., Cohen J. G., Blakeslee J. P., 2003, ApJ, 591, 850
Courteau S., Dutton A. A., 2015, ApJ, 801, L20
De Lucia G., Blaizot J., 2007, MNRAS, 375, 2
de Vaucouleurs G., de Vaucouleurs A., Corwin H. G., Jr, Buta R. J., Paturel G., Fouqué P., 1991, Third Reference Catalogue of Bright Galaxies. Volume I: Explanations and references. Volume II: Data for galaxies between 0^h and 12^h. Volume III: Data for galaxies between 12^h and 24^h. Springer-Verlag, New York
Deason A. J., Belokurov V., Evans N. W., McCarthy I. G., 2012, ApJ, 748, 2
Dekel A., Stoehr F., Mamon G. A., Cox T. J., Novak G. S., Primack J. R., 2005, Nature, 437, 707
Di Cintio A., Tremmel M., Governato F., Pontzen A., Zavala J., Bastidas Fry A., Brooks A., Vogelsberger M., 2017, MNRAS, preprint (arXiv:1701.04410)
Dutton A. A., Conroy C., van den Bosch F. C., Prada F., More S., 2010, MNRAS, 407, 2
Dutton A. A. et al., 2011, MNRAS, 416, 322
Emsellem E. et al., 2011, MNRAS, 414, 888
Forbes D. A., Romanowsky A. J., Pastorello N., Foster C., Brodie J. P., Strader J., Usher C., Pota V., 2016, MNRAS, 457, 1242
Forestell A. D., Gebhardt K., 2010, ApJ, 716, 370
Foster C. et al., 2016, MNRAS, 457, 147
Genel S., Bouché N., Naab T., Sternberg A., Genzel R., 2010, ApJ, 719, 229
Gentile G., Salucci P., Klein U., Vergani D., Kalberla P., 2004, MNRAS, 351, 903
Governato F. et al., 2010, Nature, 463, 203
Graham A. W., 2013, Elliptical and Disk Galaxy Structure and Modern Scaling Laws. Springer-Verlag, Berlin, p. 91
Harris G. L. H., Rejkuba M., Harris W. E., 2010, PASA, 27, 457
Hu W., Kravtsov A. V., 2003, ApJ, 584, 702
Johansson P. H., Naab T., Ostriker J. P., 2009, ApJ, 697, L38
Johnson R., Chakrabarty D., O'Sullivan E., Raychaudhury S., 2009, ApJ, 706, 980
Klypin A., Yepes G., Gottlöber S., Prada F., Heß S., 2016, MNRAS, 457, 4340
Koleva M., Prugniel P., de Rijcke S., Zeilinger W. W., 2011, MNRAS, 417, 1643
Kormendy J., Fisher D. B., Cornell M. E., Bender R., 2009, ApJS, 182, 216
Lange R. et al., 2015, MNRAS, 447, 2603
Läsker R., Ferrarese L., van de Ven G., 2014, ApJ, 780, 69
Macciò A. V., Stinson G., Brook C. B., Wadsley J., Couchman H. M. P., Shen S., Gibson B. K., Quinn T., 2012, ApJ, 744, L9
McDermid R. M. et al., 2015, MNRAS, 448, 3484
McLaughlin D. E., 1999, ApJ, 512, L9

Makarov D., Prugniel P., Terekhova N., Courtois H., Vauglin I., 2014, A&A, 570, A13
Moody C. E., Romanowsky A. J., Cox T. J., Novak G. S., Primack J. R., 2014, MNRAS, 444, 1475
Morganti L., Gerhard O., Coccato L., Martinez-Valpuesta I., Arnaboldi M., 2013, MNRAS, 431, 3570
Murphy J. D., Gebhardt K., Adams J. J., 2011, ApJ, 729, 129
Naab T., Johansson P. H., Ostriker J. P., 2009, ApJ, 699, L178
Napolitano N. R. et al., 2005, MNRAS, 357, 691
Napolitano N. R. et al., 2009, MNRAS, 393, 329
Napolitano N. R., Romanowsky A. J., Tortora C., 2010, MNRAS, 405, 2351
Napolitano N. R. et al., 2011, MNRAS, 411, 2035
Napolitano N. R., Pota V., Romanowsky A. J., Forbes D. A., Brodie J. P., Foster C., 2014, MNRAS, 439, 659
Navarro J. F., Frenk C. S., White S. D. M., 1996, ApJ, 462, 563
Norris M. A., Sharples R. M., Kuntschner H., 2006, MNRAS, 367, 815
Oldham L. J., Auger M. W., 2016, MNRAS, 457, 421
Oser L., Ostriker J. P., Naab T., Johansson P. H., Burkert A., 2010, ApJ, 725, 2312
Peebles P. J. E., 1982, ApJ, 263, L1
Persic M., Salucci P., Ashman K. M., 1993, A&A, 279, 343
Pillepich A. et al., 2014, MNRAS, 444, 237
Planck Collaboration XVI, 2014, A&A, 571, A16
Pota V. et al., 2013, MNRAS, 428, 389
Pota V. et al., 2015, MNRAS, 450, 3345
Raskutti S., Greene J. E., Murphy J. D., 2014, ApJ, 786, 23
Rembold S. B., Pastoriza M. G., Bruzual G., 2005, A&A, 436, 57
Remus R.-S., Dolag K., Naab T., Burkert A., Hirschmann M., Hoffmann T. L., Johansson P. H., 2017, MNRAS, 464, 3742 (Remus+17)
Richtler T., Hilker M., Kumar B., Bassino L. P., Gómez M., Dirsch B., 2014, A&A, 569, A41
Rocha M., Peter A. H. G., Bullock J. S., Kaplinghat M., Garrison-Kimmel S., Oñorbe J., Moustakas L. A., 2013, MNRAS, 430, 81
Röck B., Vazdekis A., Ricciardelli E., Peletier R. F., Knapen J. H., Falcón-Barroso J., 2016, A&A, 589, A73
Rodriguez-Gomez V. et al., 2016, MNRAS, 458, 2371
Romanowsky A. J., Douglas N. G., Arnaboldi M., Kuijken K., Merrifield M. R., Napolitano N. R., Capaccioli M., Freeman K. C., 2003, Science, 301, 1696
Romanowsky A. J., Strader J., Spitler L. R., Johnson R., Brodie J. P., Forbes D. A., Ponman T., 2009, AJ, 137, 4956
Röttgers B., Naab T., Oser L., 2014, MNRAS, 445, 1065
Samurović S., 2014, A&A, 570, A132
Samurović S., 2016, Ap&SS, 361, 199
Sánchez-Blázquez P., Gorgas J., Cardiel N., González J. J., 2006, A&A, 457, 809
Sani E., Marconi A., Hunt L. K., Risaliti G., 2011, MNRAS, 413, 1479
Schaye J. et al., 2015, MNRAS, 446, 521
Schuberth Y., Richtler T., Hilker M., Dirsch B., Bassino L. P., Romanowsky A. J., Infante L., 2010, A&A, 513, A52
Schuberth Y., Richtler T., Hilker M., Salinas R., Dirsch B., Larsen S. S., 2012, A&A, 544, A115
Scott N., Graham A. W., Schombert J., 2013, ApJ, 768, 76
Sérsic J. L., 1968, Atlas de galaxias australes. Observatorio Astronomico, Cordoba
Shen J., Gebhardt K., 2010, ApJ, 711, 484
Smith R., Choi H., Lee J., Rhee J., Sanchez-Janssen R., Yi S. K., 2016, ApJ, 833, 109
Spolaor M., Forbes D. A., Proctor R. N., Hau G. K. T., Brough S., 2008, MNRAS, 385, 675
Strader J. et al., 2011, ApJS, 197, 33
Su Y., Gu L., White R. E., III, Irwin J., 2014, ApJ, 786, 152
Taylor M. B., 2005, in Shopbell P., Britton M., Ebert R., eds, ASP Conf. Ser. Vol. 347, Astronomical Data Analysis Software and Systems XIV. Astron. Soc. Pac., San Francisco, p. 29
Terlevich A. I., Forbes D. A., 2002, MNRAS, 330, 547
Terzić B., Graham A. W., 2005, MNRAS, 362, 197
Thomas J., Saglia R. P., Bender R., Thomas D., Gebhardt K., Magorrian J., Corsini E. M., Wegner G., 2009, ApJ, 691, 770
Toloba E. et al., 2016, ApJ, 822, 51
Tortora C., Napolitano N. R., Romanowsky A. J., Capaccioli M., Covone G., 2009, MNRAS, 396, 1132
Trager S. C., Faber S. M., Worthey G., González J. J., 2000, AJ, 119, 1645
van Dokkum P. G. et al., 2008, ApJ, 677, L5
Vogelsberger M. et al., 2014, MNRAS, 444, 1518
Watkins L. L., Evans N. W., An J. H., 2010, MNRAS, 406, 264
Wechsler R. H., Bullock J. S., Primack J. R., Kravtsov A. V., Dekel A., 2002, ApJ, 568, 52
Wegner G. A., Corsini E. M., Thomas J., Saglia R. P., Bender R., Pu S. B., 2012, AJ, 144, 78
Weijmans A.-M., Krajnović D., van de Ven G., Oosterloo T. A., Morganti R., de Zeeuw P. T., 2008, MNRAS, 383, 1343
Woodley K. A., Gómez M., Harris W. E., Geisler D., Harris G. L. H., 2010, AJ, 139, 1871
Wu X., Gerhard O., Naab T., Oser L., Martinez-Valpuesta I., Hilz M., Churazov E., Lyskova N., 2014, MNRAS, 438, 2701 (Wu+14)
Zhang Z., Xu H., Wang Y., An T., Xu Y., Wu X.-P., 2007, ApJ, 656, 805
Zhang H.-X. et al., 2015, ApJ, 802, 30
Zhao D. H., Mo H. J., Jing Y. P., Börner G., 2003, MNRAS, 339, 12
Zhu L. et al., 2014, ApJ, 792, 59
Zhu L. et al., 2016, MNRAS, 462, 4001

APPENDIX A

A1 Extreme velocity anisotropy, total mass estimates and DM fractions

We investigate if the results we have obtained assuming mild velocity anisotropies are robust against extreme anisotropies, by adopting a more extreme velocity anisotropy, that is, $\beta = -1.0$. This is motivated by results from some dynamical studies (e.g. Pota et al. 2015; Zhang et al. 2015) and cosmological simulations (e.g. Röttgers et al. 2014) where such anisotropies were obtained. There are also indications from cosmological simulations (Bryan et al. 2013; Röttgers et al. 2014; Wu et al. 2014) that the stellar velocity anisotropy out to 5 R_e correlates with the fraction of stars that formed *in situ*. The nature of the reported correlation is such that in galaxies with low *in situ* stellar fractions, that is, galaxies where the late mass assembly is dominated by dry mergers, mostly the slow rotators, the anisotropy is mildly radial ($\beta > 0.2$–0.4). Galaxies with high *in situ* stellar fractions, on the other hand, show strongly tangential up to isotropic anisotropies, that is, $-1.0 \leq \beta < 0.2$. This anisotropy range is similar to what we now explore; however, GCs may not have the same velocity anisotropy as stars. From the few massive galaxies with published GC anisotropy profiles, it is difficult to pick out a clear pattern (e.g. Pota et al. 2013; Zhu et al. 2016); see also Pota et al. 2015; Zhang et al. 2015, where GCs are reported to be have strongly tangential anisotropies at large radii. More so, in the lower M_* galaxies, GC kinematics data are mostly too sparse to extract any anisotropy information; although from the PNe data associated with these galaxies, the trend is one where the PNe are isotropic near the galaxy centre and radially biased around 5 R_e. Again, PNe and GCs may not have similar anisotropies.

The top panel in Fig. A1 shows the fractional changes in M_{tot} as a function of M_* while the bottom panel shows the corresponding changes in f_{DM} versus M_*, for different anisotropy assumptions. Note that assuming a more strongly tangential anisotropy results in an increase in M_{tot} and f_{DM} only in the most mass-massive galaxies and the opposite effects in the lower M_* galaxies in our sample. If we assume a correlation between β and M_* that maximizes M_{tot} within 5 R_e, the fractional change in M_{tot} is <0.2 dex, and this

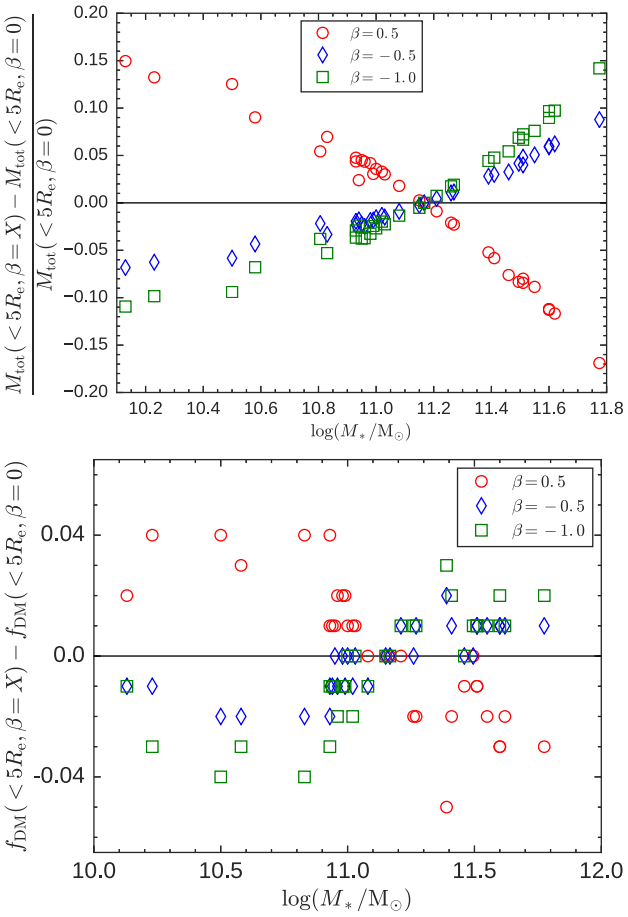

Figure A1. Top panel: fractional change in total mass within 5 $R_{\rm e}$ for different velocity anisotropy assumptions. Bottom panel: corresponding change in DM fraction within 5 $R_{\rm e}$ for different velocity anisotropy assumptions.

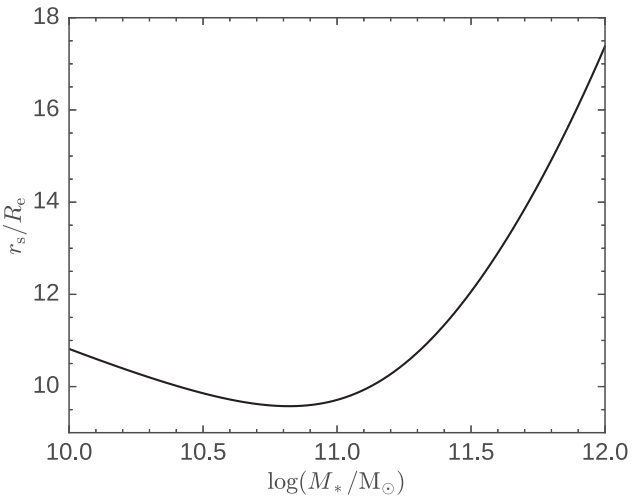

Figure A2. Top panel: variation of $r_{\rm s}/R_{\rm e}$ with stellar mass in our simple galaxy model (SGM1). The ratio of the scale radius of the DM halo to galaxy size reaches a minimum around $\log(M_*/{\rm M}_\odot) \sim 11$.

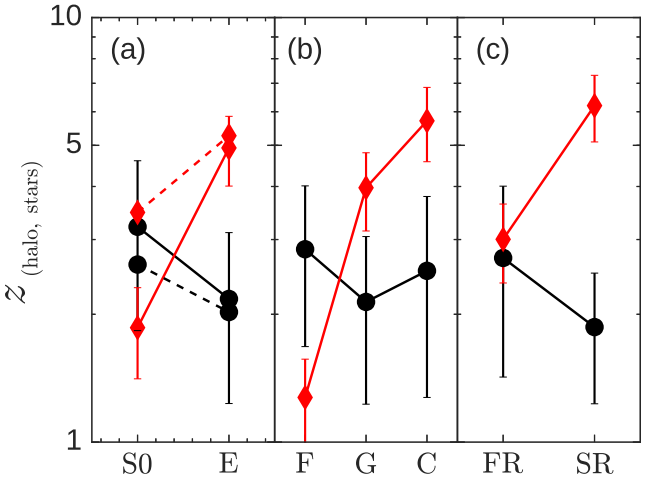

Figure A3. Summary plot showing the mean halo assembly epoch for our galaxy sample (black circles) without binning by stellar mass. The plot also shows the mean formation epoch that corresponds the luminosity-weighted ages of the central stars in our sample (red diamonds). Panel *a* shows the mean assembly epoch according to galaxy morphology (E=elliptical, S0=lenticular), with the dashed lines joining the mean epochs when galaxies with ambiguous classifications are added to either morphologies. Panel *b* shows mean assembly epoch as a function of galaxy environment (F=field, G=group, C=cluster) and panel *c* shows the mean assembly epoch as a function of central galaxy kinematics (FR=fast central rotator, SR=slow central rotator). Comparing the panels with those in Fig. 7 highlights the need to account for the strong dependence of halo assembly epoch with galaxy stellar mass. The trend we earlier observed in the field, where haloes of massive galaxies assemble at later epochs is not obvious.

results in a <0.1 change in $f_{\rm DM}$. Around $\log(M_*/{\rm M}_\odot) \sim 11$, where we measure our the lowest $f_{\rm DM}$, we now observe the least change in $M_{\rm tot}$. While it is interesting to understand the nature and systematics of GC velocity anisotropy, our analysis suggest that its effect on the total mass estimates and DM fractions within large radii is minimal.

A2 Variation of $r_{\rm s}/R_{\rm e}$ with stellar mass

This plot is in reference to how stellar mass varies with the ratio of the scale radius of the DM halo and galaxy size from our SGM1. The minimum in $r_{\rm s}/R_{\rm e}$ observed at $\log(M_*/{\rm M}_\odot) \sim 11$ implies that at this stellar mass, galaxies with may already be structurally different.

A3 Halo assembly epoch as a function of galaxy properties, without binning by stellar mass

Here, we show a version of Fig. 7, without binning our galaxies by stellar mass. We have also included galaxies with ambiguous morphological classification. Note that the late halo assembly epoch for galaxies in the field is not obvious without the correction we have applied to account for the strong dependence of $z_{\rm form}$ on galaxy stellar mass.

This paper has been typeset from a TEX/LATEX file prepared by the author.